

1 **Time-dependent cryospheric longwave surface emissivity**
2 **feedback in the Community Earth System Model**

3 **Chaincy Kuo¹, Daniel R. Feldman¹, Xianglei Huang², Mark Flanner², Ping Yang³, and**
4 **Xiuhong Chen²**

5 ¹Climate and Ecosystem Sciences Division, Lawrence Berkeley National Laboratory, Berkeley, California, USA.

6 ²Department of Climate and Space Sciences and Engineering, University of Michigan, Ann Arbor, Michigan, USA.

7 ³Department of Atmospheric Sciences, Texas A&M University, College Station, Texas, USA.

8 **Key Points:**

- 9
- 10 • The representation of longwave surface emissivity in a climate model improves its
11 cryospheric response to climate change by $+6.1 \pm 1.9$ degrees Kelvin of wintertime
12 Arctic surface temperature relative to observations.
 - 13 • Spectral emissivity kernels computed online for 200+ year model period are non-
14 linear in time and change with atmospheric water vapor.
 - 15 • Temporally and spatially localized atmospheric dynamics, captured by time-dependent
16 spectral surface emissivity kernels, expose the climatological seasonal sea-ice emis-
sivity radiative response which decreases in the Arctic with rising CO₂ forcing.

This is the author manuscript accepted for publication and has undergone full peer review but has not been through the copyediting, typesetting, pagination and proofreading process, which may lead to differences between this version and the [Version of Record](#). Please cite this article as doi: [10.1002/2017JD027595](https://doi.org/10.1002/2017JD027595)

Corresponding author: Chaincy Kuo, CKuo@lbl.gov

Abstract

Frozen and unfrozen surfaces exhibit different longwave surface emissivities with different spectral characteristics (*Feldman et al.* [2014]; *Huang et al.* [2016]), and outgoing longwave radiation and cooling rates are reduced for unfrozen scenes relative to frozen ones. Here, physically-realistic modeling of spectrally-resolved surface emissivity throughout the coupled model components of the Community Earth System Model (CESM) is advanced, and implications for model high-latitude biases and feedbacks are evaluated. It is shown that despite a surface emissivity feedback amplitude that is, at most, a few percent of the surface albedo feedback amplitude, the inclusion of realistic, harmonized longwave, spectrally-resolved emissivity information in CESM1.2.2 reduces wintertime Arctic surface temperature biases from -7.2 ± 0.9 K to -1.1 ± 1.2 K, relative to observations. The bias reduction is most pronounced in the Arctic Ocean, a region for which Coupled Model Intercomparison Project version 5 (CMIP5) models (*Taylor et al.* [2012]) exhibits the largest mean wintertime cold bias (*Flato et al.* [2013]), suggesting that persistent polar temperature biases can be lessened by including this physically-based process across model components. The ice-emissivity feedback of CESM1.2.2 is evaluated under a warming scenario with a kernel-based approach, and it is found that emissivity radiative kernels exhibit water vapor and cloud-cover dependence, thereby varying spatially and decreasing in magnitude over the course of the scenario from secular changes in atmospheric thermodynamics and cloud patterns. Accounting for the temporally-varying radiative responses can yield diagnosed feedbacks that differ in sign from those obtained from conventional climatological feedback analysis methods.

1 Introduction

The IPCC Fifth Assessment Report found that both individual models and the multi-model average surface air temperatures across the poles were significantly colder than observed (*Flato et al.* [2013]). This bias is most pronounced in the Coupled Model Intercomparison Project - Phase 5 (CMIP5) (*Taylor et al.* [2012]) multi-model distribution of Arctic Ocean wintertime surface air temperature (*Flato et al.* [2013]). This points to an underestimation of high-latitude warming by current climate models, which has profound implications both for the cryosphere and for lower latitudes (*ACIA* [2005]). This problematic situation should be rectified by identifying and fixing the sources of model error by including known physics and processes. There is growing awareness that the polar radiative energy balance is critically dependent on cloud cover and detailed cloud optical properties but that these quantities are currently poorly constrained (*Gottelman et al.* [2010]; *Kay et al.* [2012]; *English et al.* [2014]). In addition, deficiencies in our understanding of the polar radiative energy balance have been identified as contributing substantially to the under-estimation of polar climate change (*Barton et al.* [2014]).

Much effort has been expended on understanding the role of ice-albedo feedback in describing these biases. *Winton* [2006] quantify the snow albedo feedback in relation to other feedbacks to determine its impact on Arctic amplification but found that the snow albedo feedback has a negligible influence. To constrain snow albedo feedback observationally, *Qu & Hall* [2006] produce a model for the shortwave surface albedo kernel by developing an analytic model of the planetary albedo dependence on surface albedo. In a follow-up paper, the same authors derive physical models to describe the second factor in the snow albedo feedback expression: the sensitivity of snow albedo to temperature change (*Qu & Hall* [2007]). *Flanner et al.* [2011] quantify the snow albedo feedback using radiative kernels (*Soden et al.* [2008]) and northern hemisphere satellite observations of albedo and surface temperature change between 1979 and 2008. In comparison to model projections of climatological feedbacks, they found that their observational estimate of the snow albedo feedback mean was more than twice the mean value from the Coupled Model Intercomparison Project version 3 (CMIP3) models (*Meehl et al.* [2007]). *Colman*

[2013] applied surface albedo radiative kernel techniques to CMIP3 models and regressed ice-albedo feedbacks to explore northern and southern hemisphere snow/sea ice feedback relationships across seasonal, interannual, decadal, and climatological timescales, finding statistically significant correlations between temporal scales only for northern hemisphere snow albedo feedback. In a similar study contemporaneous to *Colman [2013]*, *Qu & Hall [2014]* also found that northern hemisphere snow albedo feedback exhibits strong correlations between seasonal and climatological scales in 25 CMIP5 models. In analyzing seasonal observational data records, *Crook & Forster [2014]* also found challenges in constraining climatological ice albedo feedback when considering both the northern and southern hemispheres. The average global all-sky surface albedo feedback reported in *Flato et al. [2013]*, *Colman [2013]*, and *Qu & Hall [2014]* is $0.26 \pm 0.16 \text{ W/m}^2/\text{K}$, derived from model ensembles. A multi-model mean global clear-sky surface albedo feedback is close, $0.24 \pm 0.07 \text{ W/m}^2/\text{K}$ (*Sanderson et al. [2010]*).

Despite the scientific focus on albedo feedbacks (*Winton [2006]*; *Qu & Hall [2006]*; *Qu & Hall [2007]*; *Qu & Hall [2014]*; *Flanner et al. [2011]*; *Colman [2013]*; *Crook & Forster [2014]*), the model biases relative to observations are most pronounced where there is little to no solar insolation (e.g., Arctic winter), so unless indirect wintertime processes result from a poor implementation of model albedo outside of winter, other processes must be considered to explain this persistent issue. In polar regimes the radiative energy balance is also highly sensitive to longwave emission. Recent work has shown that current climate models may be missing an important 'ice-emissivity' feedback resulting from differential snow/ice and ocean surface emissivity in the far-infrared (FIR) wavelengths (*Feldman et al. [2014]*; *Chen et al. [2014]*; *Huang et al. [2016]*). Angularly-averaged spectral emissivity (hereafter referred to simply as "emissivity") is a scaling term affecting the Planck emission of longwave radiation from materials into air, normalized by the ideal blackbody emission at the same temperature. The emissivity of materials takes on values between 0 and 1, varies spectrally, and is dependent on photon dispersion relations in the longwave, as well as on the local surface radius of curvature. For example, spectral emissivity values of frozen water in the shape of a snow grain and of an ice-slab will differ. Global circulation models (GCMs) have conventionally treated emissivity as a broadband property, but such a simplification may not be appropriate given the recent theoretical updates to spectral emissivity for a number of land surface types that show spectral dependence (*Feldman et al. [2014]*; *Chen et al. [2014]*; *Huang et al. [2016]*).

Feldman et al. [2014] discussed the potential for a positive feedback whereby lower far-infrared surface emissivity values for ocean being smaller than sea ice would lead to reduced cooling in the high latitudes as sea ice loss increases with climate change. The outgoing longwave radiation flux in high latitude and high altitude regions is particularly sensitive to spectral surface emissivity changes as the drier atmosphere in these regions is more transparent to far-infrared surface emission than in low- to mid-latitude atmospheres which have relatively higher total precipitable water. Therefore correcting the representation of radiative cooling over those regions with low precipitable water so that they exhibit a realistic characterization of surface emissivity in the models is especially important. *Chen et al. [2014]* modeled far-infrared interactions between the surface and clouds, where the surface was assigned with snow surface spectral emissivity and ice cloud scattering was taken into account. In that study, the net upward far-infrared flux at the surface and top of the atmosphere are both reduced, for a high latitude and altitude region where cloud top heights are 2-5 km above the surface.

These two aforementioned studies led to the development of a spectral surface emissivity database for weather and climate models, for which spectral emissivity is modeled for a number of surface types in the longwave from wavenumbers $0\text{-}2000 \text{ cm}^{-1}$ in *Huang et al. [2016]*; complex indices of refraction of water and ice compiled for wavelengths spanning the near ultra-violet to far-infrared (*Hale & Querry [1973]*; *Warren & Brandt [2008]*) are model inputs. Undisturbed water and ice emissivities are modeled with

Fresnel equations on a semi-infinite half-space and snow emissivities are derived by approximating snow grains as spheres, where emissivity is equal to the absorption efficiency calculated from Mie theory with optical properties adjusted to account for diffracted electromagnetic wave coherence effects when deposited snow grains are closely-packed (*Mishchenko et al.* [1994]). Spectral emissivity is dependent not only on complex indices of refraction, but on local curvature radii of longwave photon exitance as well, so spectral emissivity will evolve with snow grain size. Additionally, snow-grain size dependent spectral emissivities have been reported by *Hori et al.* [2006] and *Chen et al.* [2014]. Due to detector material cut-off responsivity, measurements of surface emissivity exist only for wavenumbers higher than 650 cm^{-1} ($\lambda < 15.4 \mu\text{m}$) (*Hori et al.* [2006]; *Baldrige et al.* [2009]), and *Huang et al.* [2016] show that modeled spectral emissivity curves compare well in this range, giving confidence to the computed emissivity values extending out to the far-infrared (wavenumbers $< 650 \text{ cm}^{-1}$).

This emissivity database can be used as part of GCM longwave radiation routines. Building on this database, *Huang et al.* [2016] explored global and regional differences between radiant energy fields in off-line simulations of the atmospheric component of the Community Earth System Model (*Hurrell et al.* [2016]) with and without realistic surface emissivity. *Huang et al.* [2016] found that the global root-mean-squared (RMS) difference in outgoing longwave radiation (OLR) between the two simulations can be as large as 2.04 W/m^2 in a summer month under clear-sky conditions.

However, to date, the effects of realistic, spectrally-resolved longwave surface emissivity on a transiently-forced, fully-coupled climate model have not been considered, so we can compare and contrast the results from including realistic surface emissivity in a model to the heretofore conventional model treatment of surface emissivity. In this paper, we will present the detailed modifications to CESM that we used to harmonize the treatment of non-unit, spectrally-resolved emissivity across all relevant model components, and then we will present an analysis of how the inclusion of realistic surface emissivity affects model polar biases. Finally, we present appropriate, computationally-efficient methods for diagnosing a GCM's ice-emissivity feedbacks and their temporal and spatial dependence, and discuss implications for the inclusion of realistic surface spectral emissivity modifications for other widely-used climate models besides CESM.

2 Methods

2.1 Emissivity specification in CESM

In the release version of CESM1, the surface components of that code calculate the grey-body broadband longwave upwelling surface flux using broadband emissivity values ϵ . Specifically in the land component, grey-body broadband longwave upwelling surface flux $F_{surf}^{\uparrow} = \epsilon \sigma_{SB} T_{ground}^4$, where σ_{SB} is the Stefan-Boltzmann constant, and T_{ground} is the ground temperature. This longwave upwelling flux is passed from the surface components into the atmospheric component, where surface emissivity contribution to the flux is retained. To preserve this contribution, CESM1 adopts a convention whereby the surface flux in the atmospheric component at the surface boundary grid, (F_{surf}^{\uparrow}), is given by σT_{rad}^4 , but T_{rad} is rederived by defining the radiative surface temperature of the model's surface components as: $T_{rad} = \sqrt[4]{F_{surf}^{\uparrow} / (\epsilon \sigma_{SB})}$, where surface emissivity is simplified to $\epsilon = 1.0$. The re-calculated radiative surface temperature, distinct from the surface temperature that other model components utilize, is used in the atmospheric component as a new temperature boundary condition for longwave flux calculations by way of the Planck function integrated over all wavelengths and angles. Consequently, calculation of upward radiative fluxes in the CESM1 release version atmospheric component amounts to a Planck curve spectral modulation of the grey-body longwave upwelling radiation of the surface components.

171 Longwave radiative fluxes are modeled by RRTMG_LW (Mlawer *et al.* [1997]), a
172 rapid radiative transfer model for use in global circulation models. RRTMG_LW uses a
173 correlated-k method with a reduced k-distribution set to calculate fluxes in global circula-
174 tion models that is at least four orders of magnitude more computationally efficient than
175 line-by-line methods. The longwave spectrum is discretized into sixteen contiguous bands
176 that balance radiometric accuracy with computational efficiency, and Table 1 lists the 16
177 discrete, contiguous spectral bands that the atmospheric component maintains for intra-
178 atmospheric radiative transfer.

179 2.2 Harmonizing emissivity across model components

180 In this work, we modify CESM1 to establish a coherent and energy-conserving treat-
181 ment of surface emissivity between all of the surface and atmospheric components of the
182 model. While we use the spectral emissivity values described by *Feldman et al.* [2014] in
183 both the atmospheric and surface interactions in CESM, the modifications we present here
184 supersede those of *Feldman et al.* [2014], which explored the sensitivity of model prog-
185 nostics to only emissivity modifications to the atmospheric component of CESM. We de-
186 tail the steps to harmonize longwave upwelling flux between the surface and atmospheric
187 components below.

188 Selecting the medium-grained snow size emissivity curve and desert scene emis-
189 sivity curve from *Huang et al.* [2016], we set the Planck-function-weighted broadband
190 emissivity for frozen surfaces (sea and land ice) over a T_s range 250-273 K to the aver-
191 age value 0.982 (deviation ± 0.0002), the corresponding value for non-vegetated miner-
192 alized land over T_s range 260-300 K is 0.926 (deviation ± 0.001), and for ocean over T_s
193 range 253-293 K is 0.908 (deviation ± 0.001). The simulated spectral surface emissivity
194 curves, Planck-function weighted broadband and original CESM1 broadband surface emis-
195 sivity values are listed in Table 1. Theoretical predictions of longwave spectral emissivity
196 beyond $15 \mu\text{m}$ for vegetation have not been undertaken at the time of this study due to
197 the lack of coherent measurements and/or modeling of plant pigment indices of refrac-
198 tion, leaf cell sizes and shapes both in its interior and epidermis, and the leaf macroscopic
199 shape. Consequently, vegetation emissivity is left unaltered from the release version of
200 CESM1, which is dependent on exposed leaf and stem area indices. Calculated in the land
201 model, upwelling longwave fluxes emitted above the canopy in vegetated grid cells are
202 preserved in the atmospheric model grid cells. Vegetated grid cells are identified in a bi-
203 nary fashion, on the condition where the sum of leaf area and stem area indices > 0.05 .
204 Medium-grained snow spectral emissivity is chosen for frozen surfaces, on both land and
205 sea-ice, inasmuch as sea-ice is only observed to be snow-free about one month per year
206 [*Warren et al.* [1999]; *Massom et al.* [2001]; *Webster et al.* [2014]].

207 In the release version of CESM1, the upward longwave surface flux is preserved in
208 the atmospheric component (Community Atmosphere Model, version 5.3) by solving for
209 surface radiative temperature as described above. While $\epsilon < 1.0$ in the land and ice com-
210 ponent in the release version of CESM1, ϵ is set to unity ($\epsilon = 1.0$) in the atmospheric
211 component, so any changes to the treatment of surface emissivity in the surface compo-
212 nents of the model requires the re-derivation of surface temperatures in the atmospheric
213 component to avoid a mismatch, and a lack of energy conservation, between the radiative
214 temperature used in the atmospheric and land, ocean, and ice components of the model.
215 However, surface temperatures in the land, ocean, and ice components are established
216 from temperature models of sub-surface layered media, therefore the surface temperature
217 re-derivation in the CESM1 release atmospheric model by applying the Stefan-Boltzmann
218 law on longwave surface upwelling flux with surface emissivity set equal to 1.0 consti-
219 tutes a distinctly different representation of surface temperature from sub-surface layered
220 temperature models.

To rectify the mismatch between atmospheric and surface model component treatments of upwelling longwave radiation, we modify CESM1 such that we pass the non-radiative surface temperature calculated in the surface components to the atmospheric component via the coupler. Radiative surface fluxes ($F_{\text{surf}}^{\uparrow}$) are determined with the updated broadband Planck-weighted emissivity in surface components in CESM1 and are merged onto the atmospheric grid in the coupler before being passed to the atmospheric component. We perform this Planck weighting using 3-point Gauss-Legendre quadrature (Li [2000]).

In our modified version of CESM1, the atmospheric component radiative temperature is set to the ground temperature reported by the land component for non-vegetated surfaces. Over ocean scenes, the sea-surface temperature from the ocean component is passed to the atmospheric component, and the atmospheric component receives proportionately-weighted ground and sea-surface temperatures for grid cells with partial land fraction. The longwave upward flux in vegetated grid cells takes into account longwave flux reflections between the canopy and ground. As such, the ground temperature in vegetated grid cells would not represent an appropriate lower boundary condition in the atmospheric model, as canopy reflections are not considered in the atmospheric model. Therefore, for grid cells of land/ocean overlap and vegetated surfaces, the radiative temperature in the atmospheric component is determined by: $T_{\text{rad}} = \sqrt[4]{F_{\text{surf}}^{\uparrow} / \sigma_{SB}}$ to preserve the upward flux determined in the surface module.

In summary, we establish the effects of the updated spectral variations in surface emissivity in model surface components that currently only support grey-body surface emissivity by creating broadband surface emissivity values through Planck-function weighting. In the atmospheric component, which does support spectrally-varying surface emissivity, the surface upward longwave fluxes calculated in the surface components persist by setting the surface radiative temperature to the ground temperature from the land component and the sea-surface temperature from the ocean component, after which RRTMG_LW calculates upwelling band-by-band fluxes with spectrally-resolved emissivity based on the scene. Discrepancies in longwave surface upwelling fluxes emanating from the different expressions between the land and atmospheric components will be quantified to legitimize the approximation.

2.3 Emissivity Radiative Response and Feedback

2.3.1 Emissivity kernels

Using our modified version of CESM1 to account for surface emissivity variations across model components realistically, we can then investigate, diagnose, and quantify the ice-emissivity feedbacks rigorously and compare them against other widely-reported feedback estimates of surface albedo. We can quantify the ice-emissivity feedback using a time-dependent radiative kernel method, whereby the temporal evolution of both the kernel and emissivity can be evaluated. The radiative kernel is an analytic expression of the partial derivative of the outgoing longwave radiation at the top of the atmosphere, taking into account its dependence on surface emissivity. The kernel can be calculated online during the integration of a global circulation model and accounts for changes in water vapor and cloud cover.

The derivation of the kernel is as follows: the sensitivity of the outgoing longwave radiation to changes in surface emissivity is quantified by the partial derivative of broadband outgoing longwave radiation (OLR) with respect to surface emissivity, and is given by:

$$\frac{\partial OLR}{\partial \epsilon}(\vec{r}, t) = \int_0^{\infty} [B(\nu, \vec{r}, T_s(\vec{r}, t)) - F^{\downarrow}(\nu, \vec{r}, t)] \Theta(\nu, \vec{r}, t) d\nu \quad (1)$$

where ϵ is emissivity, time t , and for latitude ϕ and longitude θ grid box location $\vec{r} = [\phi, \theta]$. $B(\nu, \vec{r}, T_s(\vec{r}, t))$ is the black-body function for surface temperature $T_s(\vec{r}, t)$, $F^{\downarrow}(\nu, \vec{r}, t)$

271 is the spectral downwelling flux from the atmosphere above the surface, and $\Theta(\nu, \vec{r}, t)$ is
 272 the flux transmittance from the surface to the top of the model. The sign convention for
 273 the emissivity kernel is positive for outgoing flux. $\Theta(\nu, \vec{r}, t)$ is dependent on the atmo-
 274 spheric state which is expected to evolve over CO₂ forcing periods, and includes effects
 275 of water vapor and temperature profile. The emissivity kernel can be explicitly calculated
 276 within RRTMG_LW by taking advantage of calls to its subroutines. As such, the tempo-
 277 ral emissivity kernels for both clear-sky and all-sky can be calculated online along with
 278 CESM model runs, for each grid box and time point. The kernels broken down into its
 279 spectral components $\left[\frac{\partial OLR}{\partial \epsilon}\right]_i(\vec{r}, t)$ are given by Eqn. 1 with the integration limits ν_i and
 280 ν_{i+1} , the lower and upper wavenumber band limits of RRTMG_LW band i (1).

281 We can use online analytical radiative kernel feedback methods similar to the nu-
 282 merically derived, offline radiative feedback kernel methods by *Soden et al.* [2008] and
 283 *Shell et al.* [2008], who use 3-hourly atmospheric state outputs over one model year to de-
 284 rive monthly-averaged four-dimensional (latitude, longitude, atmospheric level, and time)
 285 kernels for water vapor and lapse rate, and three-dimensional (latitude, longitude and
 286 time) surface albedo kernels using a base atmosphere from a selection of global circula-
 287 tion models (GCM). *Soden et al.* [2008] and *Shell et al.* [2008] produced these kernels for
 288 only one model year and applied the same kernels to monthly-averaged parameter pertur-
 289 bations derived over two time periods: 2000-2010 and 2100-2110, in a large number of
 290 GCM's for model feedback intercomparison. In this work, surface emissivity kernels are
 291 calculated for each atmospheric model time-step (hourly) throughout the model run period
 292 (1850-2100), but output as monthly averages for each surface grid cell. Kernel evolution
 293 as a function of time and the linear convention proposed by *Soden et al.* [2008], *Shell et al.*
 294 [2008], and *Armour et al.* [2013] can be evaluated.

295 However, the impact of non-unit surface emissivity, and changes thereof due to
 296 evolving states of the cryosphere, is strongly dependent on column-integrated atmospheric
 297 water vapor (*Feldman et al.* [2014]), and to account for this, surface emissivity kernels are
 298 calculated hourly for integrations spanning 1850-2100 and various emissions scenarios.
 299 We then use this information to produce monthly-averaged kernels for each grid box over
 300 the entire integration period, and we can use this detailed kernel calculation to evaluate
 301 kernel evolution as a function of time and test the linear convention proposed by *Soden et*
 302 *al.* [2008], *Shell et al.* [2008], and *Armour et al.* [2013].

303 2.3.2 Emissivity kernels and radiative response

304 The outgoing longwave radiation perturbation (δOLR_ϵ) due to an emissivity per-
 305 turbation $\delta\epsilon$ is the product of the kernel and $\delta\epsilon$, giving a emissivity radiative response
 306 ($EmR(\vec{r}, t)$):

$$\begin{aligned}
 307 \quad EmR(\vec{r}, t) &= -\delta OLR_\epsilon \\
 308 \quad &= -\frac{1}{A(R)} \int_R \sum_{i=1}^{16} \left[\frac{\partial OLR}{\partial \epsilon} \right]_i(\vec{r}, t) \delta\epsilon_i(\vec{r}, t) dA(r) \quad (2)
 \end{aligned}$$

309 where i is spectral emissivity in band i , in location r at time t and t_0 , for $t > t_0$, and $A(r)$
 310 is the area at location \vec{r} in the region R . $\delta\epsilon_i(\vec{r}, t) = [\epsilon_i(\vec{r}, t) - \epsilon_i(\vec{r}, t_0)]$ for an emissivity
 311 change in band i between time t and t_0 . We adopt the sign convention in such a way that
 312 emissivity radiative response is positive for a negative change in emissivity whereby out-
 313 going radiation is reduced at time t from a reference value at time t_0 , for $t > t_0$. That is,
 314 the induced radiative response due to emissivity change is positive for net incoming radia-
 315 tion.

316 2.3.3 Conventional climatological emissivity feedback

317 Following *Wetherald & Manabe* [1988], we can use conventional methods to quan-
 318 tify the feedback associated with changing surface emissivity, λ_ϵ , by looking at the top-of-

319 model longwave radiative perturbation induced by radiative forcing. This is given by the
 320 following expression:

$$321 \quad \lambda_\epsilon = -\frac{1}{A(R)} \int_R \sum_{i=1}^{16} \left[\frac{\partial OLR}{\partial \epsilon} \right]_i(\vec{r}, t) \frac{\delta \epsilon_i(\vec{r}, t)}{\delta \bar{T}_s(t)} dA(r) \quad (3)$$

$$322 \quad = -\frac{\delta OLR_\epsilon(\vec{r}, t)}{\delta \bar{T}_s(t)} \quad (4)$$

323 where $\delta \bar{T}_s(t) = \bar{T}_s(t) - \bar{T}_s(t_0)$ is the global mean surface temperature change at time t ,
 324 with respect to a reference climate model global mean surface temperature at time t_0 . The
 325 emissivity feedback component is the emissivity radiative response normalized by the
 326 global mean temperature change, and it therefore readily fits within the context of well-
 327 established climate feedback analyses.

328 Based on the forward partial radiative perturbation (PRP) technique (Wetherald &
 329 Manabe [1988]), Soden *et al.* [2008] describe their radiative kernel technique as similar
 330 to the two-sided PRP technique (Colman & McAvaney [1997]), but the kernel technique
 331 explicitly isolates the climate variable of interest. Soden *et al.* [2008] showed that climate
 332 variable feedbacks are the product of kernels calculated from a reference climate state and
 333 climate variable perturbations occurring potentially decades later. Accordingly, the Soden
 334 *et al.* [2008] kernels are derived from a reference climate at time period t_0 , so the emissiv-
 335 ity feedback from Eqn. 3 is dependent on $\left[\frac{\partial OLR}{\partial \epsilon} \right]_i(\vec{r}, t_0)$ and $\delta \epsilon_i(\vec{r}, t) = \epsilon_i(r, t) - \epsilon_i(r, t_0)$.
 336 The validity of this approach requires stationarity in $\left[\frac{\partial OLR}{\partial \epsilon} \right]_i(\vec{r}, t_0)$ over the period over
 337 which the feedback analysis is performed, which is typically multiple decades.

338 Under forced climate change scenarios, the atmospheric state and therefore $\left[\frac{\partial OLR}{\partial \epsilon} \right]_i(\vec{r}, t)$
 339 at time t , can be expected to evolve away from $\left[\frac{\partial OLR}{\partial \epsilon} \right]_i(\vec{r}, t_0)$, because water-vapor load-
 340 ing in the atmosphere follows thermodynamic constraints which modulate the strength of
 341 the emissivity feedback. Therefore, Eqn. 3 is a function of the climate state and should
 342 be time-dependent, such that λ_ϵ depends on the kernel from the future forced atmosphere
 343 $\left[\frac{\partial OLR}{\partial \epsilon} \right]_i(\vec{r}, t)$. The emissivity kernel, and in turn, the amplitude of the associated feed-
 344 back, are dependent on the kernel base state. Thus, we can evaluate temporal ice-emissivity
 345 kernels and feedback estimates using a conventional climate model feedback analysis frame-
 346 work for a forcing climate model run to test the stationarity assumption.

347 Accordingly, the surface emissivity change over a multi-decadal climatic model run
 348 between t and t_0 shall be noted as $\Delta \epsilon$ rather than $\delta \epsilon$ in Eqns. 2 and 3. We determine $\Delta \epsilon_i$
 349 in spectral band i for each grid box, year y and month m in time period t by differencing
 350 ϵ_i from the value reported over the same month and grid box over a 10-year average in the
 351 reference period t_0

$$352 \quad \Delta \epsilon_i(\vec{r}, t(m, y)) = \epsilon_i(\vec{r}, t(m, y)) - \frac{1}{10} \sum_{y=1}^{10} \epsilon_i(\vec{r}, t_0(m, y)) \quad (5)$$

353 2.3.4 Time-dependence of emissivity kernels

354 While Soden *et al.* [2008] showed that one-year's worth of kernel are adequate for
 355 multi-model ensemble feedback intercomparisons, they note that multi-year kernels could
 356 elucidate local feedback strengths, but multi-year numerical four-dimensional kernels are
 357 computationally expensive for multiple climate variables. However, since our surface emis-
 358 sivity kernel calculation has an analytic form, we can calculate these kernels online as part
 359 of the model runs to explicitly investigate regional atmospheric dynamics in the model
 360 over longer time-periods (decades) than were explored previously. As part of our analy-
 361 sis, we can therefore capture the outgoing longwave radiation perturbation at the top of
 362 the atmosphere due to surface emissivity changes, and the evolution of these effects over
 363 decadal climatological periods, as suggested by Armour *et al.* [2013].

In 2.3.3, the product of a time-dependent kernel with emissivity response and surface temperature occurring over a several decadal period intermixes the instantaneous atmospheric state used for kernel calculation with the climatological change in emissivity and surface temperature. In an analysis scheme put forth by *Armour et al.* [2013], if the atmospheric state is known at each time step and grid box, then an instantaneous emissivity radiative response is considered as the product of the time-dependent kernel with a synchronous emissivity response. Adjustments to longwave radiation due exclusively to emissivity changes from seasonal cryospheric melt and freeze cycles can be directly inferred from Eqn. 2, with t in units of months and t_0 referring to the month preceding t , so that for spectral band i , $\delta\epsilon_i$ is explicitly

$$\begin{aligned}\delta\epsilon_i(\vec{r}, t(m, y)) &= \epsilon_i(\vec{r}, t) - \epsilon_i(\vec{r}, t_0) \\ &= \epsilon_i(\vec{r}, t(m, y)) - \epsilon_i(\vec{r}, t(m-1, y)).\end{aligned}\tag{6}$$

for month m in year y . Inserting Eqn. 6 into Eqn. 2 then gives the instantaneous monthly outgoing longwave radiative emissivity response. The relative roles of the atmosphere and surface in controlling outgoing longwave radiation can be elucidated by differences in instantaneous monthly outgoing longwave radiative emissivity response between climatological eras separated by decades.

2.4 CESM run configuration

For this investigation, we use a fully-coupled CESM version 1 with Community Atmospheric Model version 5 with a nominal $2^\circ \times 2^\circ$ horizontal grid and the default time steps for each model component. To test the new emissivity values implemented in the surface and atmospheric components, we created a control run with CESM1 run under unforced conditions whereby the CO_2 concentration is set to its nominal value circa 1850, and other anthropogenic greenhouse gases and aerosols remain fixed at their respective pre-industrial levels. The model is started at 1850 and runs for 155 years. Initially, the model's top of the atmosphere net energy imbalance (net shortwave - net longwave flux) remained steady over a multidecadal run at approximately 1.2 W/m^2 . To reduce the net radiative imbalance to within $0.5\text{-}1.0 \text{ W/m}^2$ so as to be consistent with estimates of the Earth's actual radiative imbalance (*Hansen et al.* [2005]; *Trenberth et al.* [2009]), we decreased the threshold for relative humidity for low stable clouds (CESM namelist variable `cldfrc_rhmin1`) from the default value of 0.8875 to 0.8750. From this, the net radiative imbalance stabilized at $0.7 \pm 0.4 \text{ W/m}^2$ over the 155 year run period, after a spin-up time of 10 years. This model tuning adjustment was consistent with published approaches presented by *Mauritsen et al.* [2012] to reduce net radiative balance, and the tuning followed well-established tuning-parameter estimation methods (*Jackson et al.* [2008]). We call this model "1850CNTL".

With interest in model transient sensitivity relevance to the Earth's present climate (*Winton* [2006]), we also ran a forced simulation with historical CO_2 concentrations, where atmospheric CO_2 concentrations from 1850 to 1950 were scaled by the ratio of the concentration derived from Siple Station ice core data in a given year to its concentration in 1850 (*Nefel et al.* [1994]). Atmospheric CO_2 between 1976 and 2005 was set by the annually averaged Mauna Loa Observatory data (*NOAA ESRL Global Monitoring Division* [2015]), and atmospheric CO_2 between 1951 and 1975 was derived from a linear interpolation of the Siple Station and Mauna Loa datasets. Accordingly, the rate of increase of atmospheric CO_2 from 1850-1950 is approximately 0.09% per year, and from 1951-1974, it is approximately 0.24 % per year, and from 1975-2005, it is approximately 0.50% per year. The threshold for relative humidity for low stable clouds was set equal to the value specified for the control case. The historical CO_2 ramping case was run for 155 years as well for the time period 1850-2005. This model will be named "HISTCO2".

In two additional cases, atmospheres defined by representative concentration pathways defined by the Intergovernmental Panel on Climate Change (IPCC) were initiated to

415 evaluate the effect of surface emissivity on the 21st century climate. Again, the thresh-
416 old for relative humidity for low stable clouds was set equal to the value specified for the
417 1850CNTL case. We use the CESM1 fully-coupled component sets and the RCP 2.6 and
418 RCP 8.5 forcings pathways, and start the runs referencing the 2005 HISTCO2 model, and
419 integrate to 2100. These cases are simply named "RCP 2.6" and "RCP 8.5".

420 2.5 CESM output data

421 CESM model data values were averaged monthly for subsequent analysis. The `radlw.f90`
422 and `radiation.f90` code were modified to output clear-sky and all-sky spectral emissiv-
423 ity kernels, as well as the modified spectral emissivity values on the atmospheric horizon-
424 tal grid. Monthly averaged spectral emissivity kernel and emissivity maps in each of the
425 16 bands were written to the CESM history files.

426 3 Results

427 3.1 Model Validation

428 The modifications to the longwave physical representations in the model that are
429 described above can potentially destabilize the model's climate simulations, given the
430 specific tunings of the release version. For 1850CNTL, we evaluated the stability of cli-
431 matic model variables. Over the 155-year period, the net radiative imbalance was reported
432 above at $+0.7 \pm 0.4 \text{ W/m}^2$, the mean surface temperature was $287.12 \pm 0.11 \text{ K}$ with a rate of
433 change of $+1.6 \pm 2.1 \times 10^{-4} \text{ K/year}$. The sea surface temperature mean was $285.71 \pm 0.06 \text{ K}$
434 with a rate of change of $+0.9 \pm 1.1 \times 10^{-4} \text{ K/year}$. Flux differences between model compo-
435 nents are expected given that surfaces fluxes are calculated in the land model using the
436 Stefan-Boltzmann law along with Planck-averaged emissivity and surface fluxes in the
437 atmospheric model are computed with an integration of Planck function using spectral
438 emissivities. Inspection of the mean globally averaged longwave upwelling surface flux
439 difference between the atmospheric model and land model is $1.3 \pm 0.1 \times 10^{-2} \text{ W/m}^2$, with
440 a $-5.3 \pm 19.1 \times 10^{-6} \text{ W/m}^2/\text{year}$ rate of change over the 155 year model run.

441 Additionally, to benchmark our 1850 control climate against the CESM standard
442 release, we compared the surface temperature evolution of 1850CNTL against the fully-
443 coupled 1850 control run from the CESM Last Millenium Ensemble (CESM-LME, *Otto-*
444 *Bliesner et al.* [2016]), which uses the same code version (CESM1 with CAM5.3) as the
445 CESM Large Ensemble (CESM-LENS, *Kay et al.* [2015]), except that CESM-LME is
446 specified on a 2° horizontal resolution grid for the atmosphere and land surface rather
447 than the 1° for CESM-LENS. Mean surface temperature, deviation, and temperature rate
448 of change over 1850-2005 are [$287.12 \pm 0.11 \text{ K}$, $+1.6 \times 10^{-4} \text{ K/yr}$] and [$287.16 \pm 0.43 \text{ K}$,
449 $+1.18 \times 10^{-4} \text{ K/yr}$] for our 1850 control model and the CESM-LME 1850 fully coupled
450 control model, respectively. The mean temperature difference of 0.04 K is within 10%
451 of the temperature spread of 0.4 K due to internal variability in the CESM-LME mem-
452 ber. The differences in these results are not statistically-significant, so we can say that our
453 realistic surface emissivity modifications to CESM1 do not appreciably affect unforced
454 simulations.

455 3.1.1 Observational validation

456 We are interested in confronting the results of our modified and unmodified versions
457 of CESM with observations. The spectral surface emissivity treated model, designated
458 "CESM- $\epsilon(\nu)$ ", is tested against the CESM-LME (*Otto-Bliesner et al.* [2016]), for agree-
459 ment with historical (1979-2005) Arctic surface temperatures, as determined from ERA-
460 Interim (*Dee et al.* [2011]) skin temperature reanalysis.

461 Figure 1a shows a comparison of ERA-Interim skin temperatures in blue, HISTCO2
462 case of CESM- $\epsilon(\nu)$ in red, and CESM-LME in green over northern ocean latitudes from
463 1979-2005. Over the 26-year period, the mean temporally and spatially-averaged surface
464 temperature bias for CESM- $\epsilon(\nu)$ improves over 20th historical forcing CESM-LME model
465 by over 90%, from -4.4 ± 2.7 K CESM-LME mean surface temperature bias to -0.4 ± 1.6
466 K CESM- $\epsilon(\nu)$ mean surface temperature bias with respect to reanalysis data, as seen in
467 the Figure 1b residual plots. Reanalysis skin temperatures exhibit warmer mean Arctic
468 surface temperatures than the models during the wintertime with a larger winter cold bias
469 in the CESM-LME 20th century model than CESM- $\epsilon(\nu)$ ($\Delta T_S^{LME} = -7.2 \pm 0.9$ K versus
470 $\Delta T_S^{\epsilon(\nu)} = -1.1 \pm 1.2$ K in Figure 1c). Summertime model surface temperature biases to
471 skin temperature reanalysis are $\Delta T_S^{LME} = -1.1 \pm 0.4$ K and $\Delta T_S^{\epsilon(\nu)} = 0.0 \pm 0.4$ K, shown in
472 Figure 1d.

473 Mean Arctic surface temperature residuals are mapped for winter (Figures 2a and
474 2b), and summer months (Figures 2d and 2e) over 1979-2005, where the CESM-LME
475 surface temperature winter cold bias with respect to reanalysis data is most pronounced
476 (Figure 2b). In Figure 2c, modeled surface temperature difference maps show that CESM-
477 $\epsilon(\nu)$ December-January-February mean over 1979-2005 Arctic ocean surface temperature
478 is warmer than that of CESM-LME over areas of sea-ice. The cold bias pattern seen over
479 northern Eurasia in CESM-LME (Figure 2b), associated with snow-cover bias in CESM1
480 (Park *et al.* [2014]), persists in CESM- $\epsilon(\nu)$ (Figure 2a). Surface temperature over land
481 is largely unchanged between CESM- $\epsilon(\nu)$ and CESM-LME because longwave surface
482 upwelling radiation modeling over vegetated land grids in CESM-LME remained intact
483 in CESM- $\epsilon(\nu)$, as discussed in Section 2.2. The CESM- $\epsilon(\nu)$ Arctic sea-ice decline is
484 -5.9 ± 1.2 %/decade over 1950-2005, while 10 member mean CESM-LME September sea-
485 ice decline is -2.5 ± 0.4 %/decade over the same period, from 60° to 90° North; we note
486 that the uncertainty in CESM- $\epsilon(\nu)$'s sea-ice decline is much larger, being a single model
487 realization. Indeed, Stroeve *et al.* [2007] determined a September Arctic sea-ice decline of
488 -7.8 ± 0.6 %/decade over 1953-2006 observational record, whereas the multi-model IPCC
489 AR4 mean is -2.5 ± 0.2 %/decade. Improvement of Arctic sea-ice trend estimates rela-
490 tive to observations suggests that preserving and passing surface temperatures derived in
491 the surface models into the atmospheric model along with implementing spectral emissiv-
492 ity values in the atmospheric model and updated broadband surface emissivity in surface
493 models (as discussed in 2.1) improves model performance for prognosing northern hemi-
494 sphere sea-ice.

495 However, in the southern hemisphere, there is not a marked improvement between
496 CESM- $\epsilon(\nu)$ and CESM-LME. The austral summer (January, February, March) sea-ice de-
497 cline of -9.1 ± 3.7 %/decade and -7.1 ± 1.0 %/decade for CESM- $\epsilon(\nu)$ and CESM-LME
498 20th century forcing ensemble mean, respectively, are both inconsistent with observed
499 satellite data record sea-ice extent growth of $+0.95 \pm 0.23$ %/decade from 1979-2006
500 (Comiso & Nishio [2008]). These findings indicate that some combination of poorly mod-
501 eled cloud radiative effects (Lawson & Gettelman [2014]) and southern ocean dynamics
502 need to be addressed before the impacts of surface emissivity can be properly considered.

503 3.2 Emissivity and Kernels

504 3.2.1 Kernels

505 Global patterns of emissivity kernels are necessarily positive in sign and are in-
506 versely related to maps of column water. Figures 3 and 4 show clear-sky and all-sky sea-
507 sonal kernel maps, respectively, and reveal that the broadband kernels are strongest at high
508 altitude regions, dry hot climates, and high latitudes, all of which exhibit low column wa-
509 ter vapor (Feldman *et al.* [2014]). Positive trends in water vapor over high latitude oceans
510 in the summer months induce kernel amplitude suppression and can be seen in seasonal
511 all-sky kernel maps.

3.2.2 Surface emissivity evolution

Figure 5 shows the change in surface emissivity for wavenumbers in the atmospheric window (820-980 cm^{-1} , RRTMG_LW band 6) between 1850CNTL and the RCP8.5 runs at the end of the 21st Century. These maps show prominent reductions in surface emissivity (blue) at high latitudes in summer and fall seasons in the RCP8.5 run relative to the 1850CNTL run, and these reductions are collocated with increasing sea-ice melt. The maps also show increased emissivity (red) in mid- to high-latitude continental regions in winter and spring months, and we can attribute this result to increased greening of dry desert and high altitude continental regions in RCP8.5 as compared to 1850CNTL.

These maps also show the concurrent effect of sea-ice loss and changing atmospheric water vapor and clouds. The summer and fall exhibit the largest emissivity decrease over high-latitude oceans, which reduce emissivity kernel strength (Figures 3 and 4) and thereby outgoing longwave radiation at the top of the model. The inverse spatial correlation of emissivity change and transient kernel strength contributes to moderating the top-of-the-model emissivity feedback.

3.2.3 Spectrally-resolved emissivity kernels

Figure 6 shows the spectral variations in surface emissivity kernels and their relative contribution to the broadband kernel, as a function of RRTMG_LW band numbers (1). In this figure, the top row shows the clear-sky and all-sky globally-averaged spectral kernel amplitudes, and the globally-averaged spectral emissivity change from 10 years' of the 1850CNTL run is shown in the bottom row for RCP8.5 years 2090-2100. The spectral kernel shape over the RRTMG_LW bands is similar in all four CESM model runs, and the kernel amplitude in band 6 (820-980 cm^{-1}), which corresponds to the mid-infrared atmospheric window, is the dominant contributor. The shape of the spectral emissivity change highlights the differences in spectral emissivity values used for ocean and snow. Except for Band 16 (2600-3250 cm^{-1}), where $\epsilon_{\text{water}}(\nu) > \epsilon_{\text{medium-snow}}(\nu)$ for $3000 < \nu < 3250$ cm^{-1} , the emissivity of medium-snow exceeds that of ocean. Even though band 6 is the dominant contributor to the kernel, this band shows the smallest difference between ocean and medium-snow. Each of the bands 7-9 (encompassing 980-1390 cm^{-1}) exhibit comparable emissivity radiative response magnitudes to band 6. Snow emissivity values are larger than water emissivity from 980-1390 cm^{-1} for the snow grain sizes measured by Hori *et al.* [2006]. Within band 6, the emissivity of coarse snow grain sizes (800 μm median diameter) is lower than water, and consequently for this band, $\delta\epsilon_{i=6}$ would be positive under sea-ice loss.

3.2.4 Kernel temporal evolution

The temporal evolution of globally- and annually-averaged broadband clear-sky emissivity kernels for the four CESM runs are plotted as solid lines in Figure 7a, along with polynomial fits (dotted lines). The all-sky kernels are shown as ratios to clear-sky kernels in the same figure, as dashed lines, and are a little more than 50% of the clear-sky amplitude. Relative to the forced cases, the 1850CNTL kernels are temporally stable. Kernel amplitudes for CO_2 forced atmospheres are not stationary in time nor are they linear, demonstrating that by the end of the 21st century, large biases could be introduced into quantifying feedback by applying the first year's climate base state kernel. For the model specifications of this work, by the end of the 21st century the RCP8.5 scenario kernels are reduced by nearly 21% from 1850CNTL and reduced by approximately 17% from the present-day kernel (HISTCO2 at year 2005).

Figure 7b shows the globally- and annually-averaged climatological surface broadband emissivity change with respect to 1850CNTL for each CESM model run. Absolute values are less than a percent, due to globally-averaged values of surface emissivity

561 changes occurring primarily in the cryosphere (which covers about 20% of Earth's surface
562 area), much like surface albedo. In the 1850 control climate, low fluctuations around zero
563 exist for emissivity differences, which we attribute to sea-ice melt and freeze. Consider-
564 ing that ocean emissivity is lower than that of this model's designation of medium-grained
565 snow in the strong kernel RRTMG_LW band 6, negative surface emissivity change values
566 for all CO₂ forcing cases is the result of a decreased frozen surface extent in the future.

567 Over the last 10 years' of each scenario period, monthly-averaged high-latitude broad-
568 band kernel reductions relative to 1850CNTL are shown in Figure 8. HISTCO2 monthly
569 kernel amplitude temporal shape over an annual period varies by less than 3% from 1850CNTL,
570 however monthly kernel amplitudes for RCP2.6 and RCP8.5 can decrease by as much as
571 10% in clear-sky cases, and almost 30% for all-sky cases in high latitudes. This indicates
572 the problematic nature of implementing radiative kernels calculated from only one year's
573 atmospheric state in the course of analysis of the contribution of the ice-emissivity feed-
574 backs over multiple decades. We also note that the seasonal variability in high-latitude
575 kernels is highly asymmetric between the Arctic and the Antarctic. The seasonality that
576 we find in the Arctic under clear-sky conditions is largely a function of the seasonality in
577 atmospheric precipitable water vapor (Figures 9a & 9b). The all-sky seasonality is im-
578 pacted by enhanced cloud fractional coverage (Figures 9c & 9d) associated with sea-ice
579 loss, which has been consistently observed in CMIP3 and CMIP5 models (*Karlsson et*
580 *al.* [2013]). In the Antarctic, however, the clear-sky kernel reduction is largely invariant
581 through the seasons, except for the end of the century RCP8.5 case, where the southern
582 winter warms.

583 The monthly evolution of spectral kernels for high latitudes for the last 10 years'
584 of the RCP 8.5 scenario is shown in Figure 10. Figures 10a and 10b show the monthly
585 kernel amplitude for northern high latitude clear-sky and all-sky conditions, respectively,
586 and are affected by the seasonality in water vapor (Figure9). The effects of ozone in the
587 southern high latitudes can also be seen in bands 6 and 7, where rising O₃ concentrations
588 in the winter months decrease the kernel strength, and are shown in Figures 10c and 10d
589 for clear- and all-sky conditions, respectively. RRTMG_LW bands 2 and 3, in the water-
590 vapor rotational absorption feature shows the most pronounced seasonality due to the sea-
591 sonality in column water-vapor.

592 The climatological spectral surface emissivity change $\Delta\epsilon_i(t)$ (Eqn. 5) relative to
593 1850CNTL is plotted for each month in a ten-year average of years 2090-2100 of RCP 8.5
594 in Figures 11a and 11b, at northern and southern high latitudes, respectively. The clima-
595 tological surface emissivity change for the end of the century RCP 8.5 scenario is negative
596 for all months and RRTMG_LW bands except springtime high northern latitudes band 16,
597 where ocean emissivity is larger than medium-grained snow emissivity above 3000 cm⁻¹.
598 The climatological surface emissivity change is largest in the summer and early autumn
599 in high northern latitudes, indicating increased thaw during the typical Arctic melt sea-
600 son. The weak spectral surface emissivity change in the springtime indicates wintertime
601 Arctic sea-ice coverage persistence (75% of pre-industrial) even at the end of the century
602 in RCP8.5. In the southern high latitudes, the climatological spectral surface emissivity
603 change is the most negative during the winter months, during which climatological surface
604 temperature increase is also largest (60% relative to HISTCTL).

605 Focusing on the last 10 years' of the RCP 8.5 scenario, the average seasonal spectral
606 surface emissivity change, $\delta\epsilon_i(t)$ (Eqn. 6), contribution to the surface radiative response
607 from month-to-month is seen in Figures 11c and 11d, again for northern and southern
608 high latitudes respectively. Cryospheric phase changes can be observed in the seasonal cy-
609 cle emissivity change between the northern and southern high latitudes, with freezing pe-
610 riods producing positive $\delta\epsilon_i(t)$ and negative $\delta\epsilon_i(t)$ for melt periods. Atmospheric dynamics
611 effects on phase changes are evident from structure in Figure 11c, where continental and
612 ocean current spatial distribution in the Arctic impose complexity. In contrast, consistent
613 transitions throughout the bands and months occur in the Antarctic (Figure 11d), where

614 cryospheric changes are more established on sea-ice. Note that the $\delta\epsilon_i(t)$ amplitudes deter-
615 mined here are a product of the assigned spectral emissivity values for water and medium-
616 grained snow, which is a simplification for seasonal emissivity values of frozen surfaces.
617 Snow-cover on ice sheets will evolve from fine-grained deposition in the cold and windy
618 months to coarse-grains as seasonal temperatures rise. While not a focus in this study,
619 the foundation for surface emissivity feedback analysis incorporating seasonal snow grain-
620 size dependent spectral emissivity has been built with this work.

621 3.3 Emissivity feedbacks

622 3.3.1 Conventional feedback analysis

623 To put the emissivity feedback magnitude into the context of conventional climate
624 feedback analysis, we first report the global emissivity feedback, λ_ϵ , as one component
625 of the total feedback parameter λ , as defined by *Wetherald & Manabe* [1988]. In this
626 form, the emissivity radiative response relative to pre-industrial period is normalized by
627 the global mean temperature change. Noting the surface emissivity kernel evolution due,
628 largely, to water vapor dependence, we show the feedback on the 1850CNTL model by
629 calculating surface emissivity kernels from the 1850CNTL, as well as referencing $\Delta\epsilon_i(\vec{r}, t)$
630 with t_0 as the 1850CNTL period.

631 Zonally and temporally-averaged cryosphere emissivity feedbacks are shown in Fig-
632 ure 12 with conventional feedback analysis. The globally-averaged surface temperature dif-
633 ference $\Delta\bar{T}_S$ in each scenario was obtained by subtracting a 1850CNTL 10-year averaged
634 monthly global mean surface temperature from monthly surface temperature of each sce-
635 nario over a 10 year period, ending at the year appearing in the Figure 12 legend. In the
636 four scenarios starting with present-day, the climatological emissivity response, $\Delta\epsilon_i(\vec{r}, t)$
637 is determined by differencing ϵ at each spectral band, year, month and grid cell in these
638 10 year periods with a 10-year averaged 1850CNTL spectral ϵ for each month and grid
639 cell. Feedback analysis is only considered in a spatio-temporal grid point for which $\Delta\bar{T}_S$
640 is significant, that is, when $\Delta\bar{T}_S > \sigma_{T_S}$, where σ_{T_S} is the surface temperature standard
641 deviation over the 10-year period for a particular month. Therefore feedbacks are zonally
642 and temporally averaged by the number of contributing non-zero grid values. Insignificant
643 $\Delta\bar{T}_S$'s may occur for HISTCO2, but are generally avoided in the future CO₂ forcing sce-
644 narios. Grid cells for which CESM history field ICEFRAC or FRACSNO contained values
645 > 0.0 for any monthly-averaged timepoint over the analysis period were considered to be
646 members of the cryosphere. Feedbacks for HISTCO2 are much larger than the forced runs
647 due to $\Delta\bar{T}_S$ values which are small and somewhat unstable compared to those of future
648 forcing scenarios. Sea-ice emissivity global mean feedback amplitude is stable with in-
649 creasing future CO₂ forcing due to linear kernel strength scaling with rising global mean
650 temperature, and mean zonal broadband $\Delta\epsilon$ amounting to $\mathcal{O}(10^0)$ %. However, the spa-
651 tial distribution of increasing feedback moves poleward, which is consistent with increased
652 sea-ice melt at higher latitudes. Our diagnosed ice-emissivity feedbacks can then be com-
653 pared to other well-known feedbacks, such as that due to surface albedo (*Hall&Qu* [2006];
654 *Winton* [2006]; *Flanner et al.* [2011]; *Crook & Forster* [2014]; *Armour et al.* [2013]). We
655 do note that the all-sky emissivity feedback is dependent on clouds, which will complicate
656 the feedback analysis.

657 Considering the nonlinearity of the emissivity kernels, we compare feedback cal-
658 culations based on static kernels $K(t_{\text{ref}})$ (where t_{ref} is the reference time period) against
659 those calculated with time-dependent/dynamic kernels $K(t)$ to look at calculation biases
660 with respect to agreement between methods. For each CO₂ forced case, surface emissivity
661 feedbacks are computed for increasing specification: from global, cryospheric, to sea-ice
662 emissivity feedbacks; the latter two separated into northern and southern hemispheres (0°
663 to 90° latitude and -90° to 0° latitude). When comparing different reference periods in
664 static kernel use (Figure 13a), in which both the static kernels and climatological emissiv-

ity change differ, the mean bias between surface emissivity feedback calculation methods is 1.16×10^{-3} W/m²/K. When comparing surface emissivity feedbacks calculated using static kernels against using time-dependent kernels (Figure 13b) for the same reference period the bias is almost twice as large at 1.95×10^{-3} W/m²/K. The use of time-dependent kernels in feedback calculations (Figure 13c) the mean bias between different reference periods is reduced down to 8.01×10^{-4} W/m²/K (compare to Figure 13a). In the previous three cases, surface emissivity feedback was calculated in the conventional method, relative to the global mean surface temperature change.

We must also consider the appropriateness of using global mean surface temperature change for high-latitude feedbacks. While surface albedo feedback studies such as *Bony et al.* [2006], *Sanderson et al.* [2010], and *Winton* [2006] normalized the surface radiative response with respect to global mean surface temperature change, *Hall & Qu* [2006], *Flanner et al.* [2011], *Colman* [2013] *Crook & Forster* [2014], and *Qu & Hall* [2014] have implemented regional surface temperature change in their formulation of surface albedo feedback to compare seasonal to climatological surface albedo feedback. By using zonal mean surface temperature change as $\Delta \bar{T}_S$ in Eqn. 3, we find minimal bias (-1.72×10^{-4} W/m²/K) when using time-dependent kernels, as shown in Figure 13d, where we compare pre-industrial and present-day kernel calculations. Indeed with the smallest bias, Figure 13d shows that the determination of the surface emissivity feedback should be based on the localized surface temperature change rather than the global surface temperature change, in order to provide a more physically mechanistic formulation of this feedback. The biases in Figures 13a-d are respectively then 43%, 72%, 29%, and 6% of the mean global sea-ice emissivity feedback calculated by time-dependent kernels with normalization with zonal mean surface temperature change. The largest bias occurs in the case comparing emissivity feedbacks calculated by static versus time-dependent radiation kernels normalized by climatological global mean temperature differences (Figure 13b), and smallest feedback bias exists when applying time-dependent kernels normalized by mean zonal temperature changes from different reference periods (Figure 13d).

Directing attention to frozen and unfrozen water surfaces, for which theoretical long-wave emissivity values were derived by co-authors in *Chen et al.* [2014] and *Huang et al.* [2016], we list globally-averaged sea-ice emissivity feedback values derived from static kernels and time-dependent/dynamic kernels in Table 2. Surface emissivity feedback values are also separated in the table by two methods of surface temperature change: the global mean surface temperature difference and zonal mean surface temperature difference. Static surface emissivity kernels, surface emissivity change, and surface temperature change are referenced to the 1850CNTL atmosphere. Parameter standard deviations over the 10-year periods are propagated into feedback uncertainties expressions for each of the four feedback calculation types. Focusing the discussion to future forcing scenarios, clear-sky sea-ice surface emissivity feedbacks determined with dynamic kernels are on the order of 90% of those determined with static kernels, and all-sky dynamic kernel sea-ice emissivity feedbacks are less than 60% of static kernel derived values. Normalizing by the zonal mean surface temperature difference, mechanistically more physical, reduces the sea-ice surface emissivity feedback values by roughly 50%, compared to normalization by the global mean surface temperature difference. As the most physical method in Table 2, time-dependent kernel feedback calculation with normalization by zonal mean surface temperatures produce clear-sky sea-ice emissivity feedback values that are less than 50% of values when calculated with static kernels and with normalization by global mean surface temperature difference. For all-sky, time-dependent kernel, zonal mean surface temperature derived sea-ice emissivity feedback values are less than 30% of static kernel, global mean surface temperature feedback values.

Surface emissivity feedbacks for CO₂ forcing scenarios referenced to 1850CNTL and calculated with their respective time-dependent clear- and all-sky kernels are shown in Figure 14 for northern and southern hemispheric, and global means, for which mean

718 surface temperature change is calculated zonally. Northern hemisphere cryosphere in-
719 cludes snow-covered land, and as vegetated areas become more exposed in the RCP 21st
720 century CO₂ forcing scenario wintertime, surface emissivity feedbacks are negative for
721 $\epsilon_{\text{veg}} > \epsilon_{\text{snow}}$, yet increase with forcing strength. The southern hemisphere cryosphere sur-
722 face emissivity feedbacks are due to changes in the distribution of sea-ice, as their values
723 are equivalent to the sea-ice emissivity feedback; they are exclusively positive, denoting
724 sea-ice melt in future scenarios compared to the reference period. Despite undergoing less
725 sea-ice melt, southern hemisphere cryosphere/sea-ice emissivity feedbacks are larger in
726 amplitude than northern hemisphere feedbacks due to the larger southern hemisphere sea-
727 ice surface area. For both hemispheres, the sea-ice surface emissivity feedback is stable
728 throughout the forcing scenarios as indicated by feedback calculations for the last 10-years
729 of each scenario period. Driving this stability is that the time-dependent sea-ice emissivity
730 radiative response is counterbalanced by zonally-averaged surface temperature change (eg.,
731 Figure 13).

732 3.3.2 Seasonal response analysis

733 Time-dependent emissivity kernels allow us to discern the longwave radiative re-
734 sponse of the climate to emissivity changes at time t by examining the emissivity radi-
735 ative response over the seasonal cycle. Figure 15 plots 10-year averaged emissivity ker-
736 nels, month-to-month emissivity change ($\delta\epsilon_{i=6}$), and emissivity radiative response for
737 RRTMG_LW band 6 in each column; the top row for sea-ice dominant northern latitudes,
738 and the bottom row for sea-ice dominant southern latitudes. We inspect the atmospheric
739 dynamics, melt/freeze cycle, and emissivity radiative response in these high latitude re-
740 gions as they evolve with increased CO₂ forcing.

741 At high northern latitudes, Figure 15a shows that, due to water vapor, emissivity
742 kernels in winter-time allow more longwave radiation to escape the top of the atmosphere
743 than summertime, for RRTMG_LW band 6. Despite a month-to-month emissivity change
744 ($\delta\epsilon_{i=6}$) with an amplitude larger during melt than freeze periods in future CO₂ forcing
745 scenarios (Figure 15b), the combination of seasonal atmospheric effects on the emissivity
746 kernel and melt/freeze cycle produces a seasonal emissivity radiative response in Figure
747 15c, which cumulatively over the year is negative in sign (Figure 16). Examination of
748 contributing factors show that the Arctic emissivity kernel amplitude difference between
749 warm and cold seasons becomes larger with increasing CO₂ forcing scenarios, impacting
750 the differential between summertime and wintertime emissivity radiative response. Month-
751 to-month emissivity changes also evolve with increased CO₂ forcing, with an earlier onset
752 springtime melt. However, the winter-time refreeze (February/March) maximum produces
753 a rebound effect that is as large as 84% of pre-industrial levels, even at the end of the
754 21st century. Again, however, the seasonality of the emissivity kernels as shown in Figure
755 16 stands in contrast to the annually-averaged emissivity radiative response.

756 In the Antarctic, the seasonal emissivity kernel strength (Figure 15d) is influenced
757 by ozone concentration more than water vapor and therefore dips in the southern winter
758 during increased ozone concentration and low water vapor. Thus, the RRTMG_LW band
759 6 kernels have higher amplitude during the melt season where emissivity changes are neg-
760 ative (Figure 15e). Another feature of note is that for all cases, the southern atmosphere
761 over the sea-ice dominant latitudes does not change significantly from the 1850CNTL at-
762 mosphere, thereby larger amplitude emissivity changes in the future CO₂ forcing scenarios
763 impose a stronger impact than emissivity kernels in the emissivity radiative response (Fig-
764 ure 15f).

765 The climatological evolution of seasonal emissivity radiative response (Eqn. 2) can
766 be seen in Figure 16, where we plot 10-year zonal and annual averages of the seasonal
767 emissivity response (annual average of plots such as Figs. 15c and 15f for each latitude).
768 The emissivity radiative response at high northern latitudes shows increasing outgoing ra-

769 diation with CO₂ forcing, given the seasonal atmospheric dynamics and surface emissivity
770 change oscillation between positive and negative sign. In the southern ocean, the emissiv-
771 ity radiative response in future CO₂ forcing scenarios reduces, signifying positive clima-
772 tological seasonal emissivity radiative response, given climatologically stable atmospheric
773 dynamics over the southern ocean and modeled climatological decrease in frozen surfaces.
774 Bear in mind that Antarctic sea-ice decline is simulated in the CESM models to be much
775 faster than observations, as discussed in Section 3.1.1.

776 Even though we do not make direct comparisons of seasonal with climatological
777 emissivity feedback here, we note the relative sign of the emissivity radiative responses
778 between the periods. The climatological sea-ice emissivity radiative response (use of Eqn.
779 5 in Eqn. 2) is positive, given the climatological decrease in summertime frozen surfaces
780 and emissivity values for frozen and non-frozen surfaces specified in this work. However,
781 on short time scales, the seasonal sea-ice emissivity radiative response (Eqn. 6 in Eqn. 2),
782 is about an order of magnitude less than the climatological emissivity radiative response
783 and is consistently negative. Focusing on northern high latitudes, the climatologically ac-
784 cumulated seasonal sea-ice emissivity radiative response remains negative. The northern
785 high latitude emissivity radiative response is influenced by two components: first is the
786 declining sea ice, and secondly, the climatologically evolving seasonal emissivity radiative
787 kernels modulate the strength of the emissivity reduction during springtime/summertime
788 melt, as shown in Figure 15a. In the southern high latitudes over sea ice, the climatologi-
789 cal emissivity radiative response is driven by predominantly the surface emissivity differ-
790 ences due to declining sea ice, as water vapor has less seasonal impact on the emissivity
791 radiative kernel than in the northern atmosphere, and therefore the southern high latitude
792 climatological emissivity radiative response is positive.

793 4 Discussion and Conclusions

794 We have investigated how the inclusion of realistic and consistent surface emissivity
795 in both land-surface and atmospheric components of the CESM coupled-climate model af-
796 fects a wide range of climate variables. We did this by replacing the broadband emissivity
797 values in RRTMG_LW for water, medium-grained snow, and desert scenes. We find that
798 this harmonized treatment of surface emissivity within CESM can be important for reduc-
799 ing high-latitude temperature biases. We also find that short-term effects of atmospheric
800 dynamics and spectral information need to be considered to understand radiative effects
801 in higher detail, and are possible with radiative kernels computed for every grid and time
802 point for the entire model integration period.

803 We performed feedback analysis and found that sea-ice emissivity feedback is posi-
804 tive in sign, which is driven by the differences in emissivity between frozen and unfrozen
805 surfaces at wavenumbers less than 3000 cm⁻¹. From this single mean state realization rep-
806 resented by our transient model, we have quantified the global sea-ice emissivity feedback
807 in an atmosphere at year 2100 in the RCP 8.5 scenario as $+8.05 \pm 0.15 \times 10^{-3}$ W/m²/K
808 for clear-sky and $+2.62 \pm 0.15 \times 10^{-3}$ W/m²/K for all-sky, with uncertainties derived from
809 propagation of Eqn. 3 variables' 1- σ deviations over the analysis time period. The global
810 clear-sky sea-ice emissivity feedback is a few percent of surface albedo feedback, and
811 this relative amplitude is not unexpected, given that albedo change (tens of %) is much
812 larger than emissivity change (a few %), between snow and water. This feedback anal-
813 ysis used spectrally-resolved kernels and revealed time-varying interactions between the
814 bands. We can extend this analysis to diagnose the ice-emissivity feedback in other earth
815 system models with offline calculations of spectral surface emissivity radiative kernels and
816 spectral surface emissivity change for models with sea-ice fraction output.

817 We also note that conventional climatological feedback calculations indicate that
818 this sea-ice emissivity feedback is positive in sign, but that the radiative effects of the dif-
819 ference in emissivity between frozen and unfrozen surfaces exhibit seasonal dependence.

820 Furthermore, this seasonality itself exhibits meridional asymmetry due to differences in
821 sea-ice response to climate forcing between the Arctic and the Antarctic. In the Arctic,
822 this seasonal, temporally higher order analysis exhibits increasing outgoing surface emis-
823 sivity radiative response in a warming climate. While the sea-ice emissivity feedback and
824 seasonal sea-ice emissivity radiative response amplitudes are a few percent of surface
825 albedo feedbacks, the feedback analysis methods outlined in this work demonstrate that
826 spatially and temporally localized feedback analysis can give insight into the mechanisms
827 at work on those scales which differ in amplitude and sign from conventional climato-
828 logical analyses. This is demonstrated in Section 3.3.2, where by executing seasonal sur-
829 face emissivity response analysis with time-dependent kernels and time-dependent surface
830 emissivity change, the northern high latitude climatological surface emissivity radiative re-
831 sponse is negative while southern high latitude climatological surface emissivity radiative
832 response is positive. In the presence of sea ice decline, the Arctic atmospheric dynam-
833 ics develops in such a way that the climatological surface emissivity radiative response
834 is negative, whereas the Antarctic atmospheric dynamics is rather static over the climato-
835 logical forcing periods, giving way to positive climatological surface emissivity radiative
836 response. Additionally, the sign between high latitude climatological surface emissivity
837 radiative response analysis and conventional emissivity feedback analysis can differ if the
838 latter case does not capture underlying driving feedback mechanisms present in a higher
839 order domain.

840 The inclusion of this realistic physics leads to improved agreement between CESM
841 model results and Arctic surface temperatures and sea-ice trends. This reduction of persis-
842 tent surface temperature biases suggests that modeling surface emissivity may be a con-
843 tributing factor to cold-pole model biases, where radiative surface temperatures would
844 constantly being rederived low in RRTMG_LW compared to surface components, when
845 surface emissivity is set to 1.0 in the atmospheric component. To clarify, the CESM1 re-
846 lease version calculates two distinct representations of the surface temperature: the surface
847 temperature derived from sub-surface temperature profile models residing in surface model
848 components, and the surface temperature calculated by the Stefan-Boltzmann law with
849 surface emissivity set equal to 1.0. We tried to reconcile the disparate representation of
850 surface temperature to ultimately harmonize the treatment of surface temperature and ra-
851 diative fluxes. With spectral surface emissivity modeling as outlined in Section 2.2, more
852 realistic calculated longwave upward and downward fluxes impact energy balance and sur-
853 face temperature derivations in the surface components in the next time-step. Twenty-four
854 atmospheric GCMs that participated in the CMIP5 (*Taylor et al. [2012]*) assume constant
855 surface emissivity over the entire longwave spectrum, and so the modifications to CESM1
856 presented here may be relevant for those models.

857 There is still work to be done regarding ice-emissivity feedback analysis, however.
858 First, in these simulations the downward longwave radiative flux still remains decoupled
859 from the ocean model, though we should note that the influence of this decoupling on
860 the results presented here is likely to be small because the longwave extinction coeffi-
861 cient amplitude excludes longwave radiation from transmission beyond the first ocean layer
862 (W. Large, National Center for Atmospheric Research, *personal communication*). Second,
863 the treatment of spectral surface emissivity for vegetated surfaces is incomplete in that its
864 variation based on plant species and far-infrared emissivity for any vegetated scenes is un-
865 known. Third, the dependence of the ice-emissivity feedback on snow grain-size needs to
866 be explored. We used the spectral emissivity curve for medium-grained snow, but several
867 studies have noted a decrease in emissivity with snow grain-size that is spectrally-variable
868 (*Hori et al. [2006]; Huang et al. [2016]*). Therefore, the sign of the seasonal surface emis-
869 sivity radiative response and the climatological surface emissivity feedback could depend
870 on the details of snow metamorphosis, which further motivates the need for realistic mod-
871 eling of snow grain-size evolution both in the sea-ice and land components of coupled-
872 climate models. Finally, a similar analysis to what is presented here for CESM will need

873 to be performed in other climate models to establish if surface-emissivity physics are im-
874 portant for high-latitude feedbacks and bias reduction in the multi-model ensemble.

875 Acknowledgments

876 We would like to extend our gratitude to Drs. Gautam Bisht, William Riley, Marika
877 Holland, Stephen Yeager, and Elizabeth Hunke for their helpful input, and the anonymous
878 reviewers for their careful evaluation of this work. This material is based upon work sup-
879 ported by the U.S. Department of Energy, Office of Science, Office of Biological and En-
880 vironmental Research, Scientific Discovery through Advanced Computing, under contract
881 number DE-AC02-05CH11231. The authors used resources of the National Energy Re-
882 search Scientific Computing Center (NERSC), a DOE Office of Science User Facility sup-
883 ported by the Office of Science of the U.S. Department of Energy under that same award.
884 Model output data can be found at
885 <http://portal.nersc.gov/project/m2250/emissfdbk/>

886 References

- 887 ACIA, 2005. Arctic Climate Impact Assessment. ACIA Overview report. Cambridge Uni-
888 versity Press. 1020 pp., ISBN 0 521 86509 3
- 889 Armour, K. C., Bitz, C. M., & Roe, G. H. (2013). Time-varying climate sensitivity from
890 regional feedbacks. *Journal of Climate*, 26(13), 4518-4534.
- 891 Baldrige, A. M., Hook, S. J., Grove, C. I., & Rivera, G. (2009). The ASTER spectral
892 library version 2.0. *Remote Sensing of Environment*, 113(4), 711-715.
- 893 Barton, N. P., Klein, S. A., & Boyle, J. S. (2014). On the contribution of longwave radi-
894 ation to global climate model biases in Arctic lower tropospheric stability. *Journal of*
895 *Climate*, 27(19), 7250-7269.
- 896 Bony, S., Colman, R., Kattsov, V.M., Allan, R.P., Bretherton, C.S., Dufresne, J.L., Hall,
897 A., Hallegatte, S., Holland, M.M., Ingram, W. and Randall, D.A. (2006). How well do
898 we understand and evaluate climate change feedback processes?. *Journal of Climate*,
899 19(15), 3445-3482.
- 900 Chen, X., Huang, X., & Flanner, M. G. (2014). Sensitivity of modeled far-IR radiation
901 budgets in polar continents to treatments of snow surface and ice cloud radiative proper-
902 ties. *Geophysical Research Letters*, 41(18), 6530-6537.
- 903 Colman, R. A., & McAvaney, B. J. (1997). A study of general circulation model climate
904 feedbacks determined from perturbed sea surface temperature experiments. *Journal of*
905 *Geophysical Research: Atmospheres*, 102(D16), 19383-19402.
- 906 Colman, R. A. (2013). Surface albedo feedbacks from climate variability and change.
907 *Journal of Geophysical Research: Atmospheres*, 118(7), 2827-2834.
- 908 Comiso, J. C., & Nishio, F. (2008). Trends in the sea ice cover using enhanced and
909 compatible AMSR-ÅRE, SSM/I, and SMMR data. *Journal of Geophysical Research:*
910 *Oceans*, 113(C2).
- 911 Crook, J. A., & Forster, P. M. (2014). Comparison of surface albedo feedback in climate
912 models and observations. *Geophysical Research Letters*, 41(5), 1717-1723.
- 913 Dee, D.P., Uppala, S.M., Simmons, A.J., Berrisford, P., Poli, P., Kobayashi, S., Andrae, U.,
914 Balmaseda, M.A., Balsamo, G., Bauer, P. & Bechtold, P. (2011). The ERA-Interim
915 reanalysis: Configuration and performance of the data assimilation system. *Quarterly*
916 *Journal of the royal meteorological society*, 137(656), pp.553-597.
- 917 English, J.M., Kay, J.E., Gettelman, A., Liu, X., Wang, Y., Zhang, Y. & Chepfer, H.,
918 2014. Contributions of clouds, surface albedos, and mixed-phase ice nucleation schemes
919 to Arctic radiation biases in CAM5. *Journal of Climate*, 27(13), pp.5174-5197.
- 920 Feldman, D. R., Collins, W. D., Pincus, R., Huang, X., & Chen, X. (2014). Far-infrared
921 surface emissivity and climate. *Proceedings of the National Academy of Sciences*,
922 111(46), 16297-16302.

- 923 Flanner, M. G., Shell, K. M., Barlage, M., Perovich, D. K., & Tschudi, M. A. (2011). Ra-
924 diative forcing and albedo feedback from the Northern Hemisphere cryosphere between
925 1979 and 2008. *Nature Geoscience*, 4(3), 151-155.
- 926 Flato, G., Marotzke, J., Abiodun, B., Braconnot, P., Chou, S. C., Collins, W. J., Cox, P.,
927 Driouech, F., Emori, S., Eyring, V. & Forest, C.(2013). Evaluation of Climate Models.
928 In: *Climate Change 2013: The Physical Science Basis. Contribution of Working Group
929 I to the Fifth Assessment Report of the Intergovernmental Panel on Climate Change.*
930 *Climate Change 2013*, 5, 741-866.
- 931 Gettelman, A., Liu, X., Ghan, S.J., Morrison, H., Park, S., Conley, A.J., Klein, S.A.,
932 Boyle, J., Mitchell, D.L. & Li, J.L. (2010). Global simulations of ice nucleation and ice
933 supersaturation with an improved cloud scheme in the Community Atmosphere Model.
934 *Journal of Geophysical Research: Atmospheres*, 115(D18).
- 935 Hale, G. M., & Querry, M. R. (1973). Optical constants of water in the 200-nm to 200-
936 μm wavelength region. *Applied optics*, 12(3), 555-563.
- 937 Hall, A., & Qu, X. (2006). Using the current seasonal cycle to constrain snow albedo
938 feedback in future climate change. *Geophysical Research Letters*, 33(3).
- 939 Hansen, J., Nazarenko, L., Ruedy, R., Sato, M., Willis, J., Del Genio, A., Koch, D., Lacis,
940 A., Lo, K., Menon, S. & Novakov, T. (2005). Earth's energy imbalance: Confirmation
941 and implications. *Science*, 308(5727), 1431-1435. doi:10.1126/science.1110252
- 942 Holland, M. M., & Bitz, C. M. (2003). Polar amplification of climate change in coupled
943 models. *Climate Dynamics*, 21(3-4), 221-232.
- 944 Hori, M., Aoki, T., Tanikawa, T., Motoyoshi, H., Hachikubo, A., Sugiura, K., ... & Taka-
945 hashi, F. (2006). In-situ measured spectral directional emissivity of snow and ice in the
946 8-14 μm atmospheric window. *Remote Sensing of Environment*, 100(4), 486-502.
- 947 Huang, X., Chen, X., Zhou, D. K., & Liu, X. (2016). An Observationally Based Global
948 Band-by-Band Surface Emissivity Dataset for Climate and Weather Simulations. *Jour-
949 nal of the Atmospheric Sciences*, 73(9), 3541-3555.
- 950 Hurrell, J. W., Holland, M. M., Gent, P. R., Ghan, S., Kay, J. E., Kushner, P. J., Lamar-
951 que, J.F., Large, W.G., Lawrence, D., Lindsay, K. & Lipscomb, W. H. (2013). The
952 community earth system model: a framework for collaborative research. *Bulletin of the
953 American Meteorological Society*, 94(9), 1339-1360.
- 954 Iacono, M. J., Mlawer, E. J., Clough, S. A., & Morcrette, J. J. (2000). Impact of an im-
955 proved longwave radiation model, RRTM, on the energy budget and thermodynamic
956 properties of the NCAR community climate model, CCM3. *Journal of Geophysical Re-
957 search*, 105(D11), 14873-14890.
- 958 Jackson, C. S., Sen, M. K., Huerta, G., Deng, Y., & Bowman, K. P. (2008). Error reduc-
959 tion and convergence in climate prediction. *Journal of Climate*, 21(24), 6698-6709.
- 960 Karlsson, J., & Svensson, G. (2013). Consequences of poor representation of Arctic sea-
961 ice albedo and cloud-radiation interactions in the CMIP5 model ensemble. *Geophysical
962 Research Letters*, 40(16), 4374-4379.
- 963 Kay, J.E., Hillman, B.R., Klein, S.A., Zhang, Y., Medeiros, B., Pincus, R., Gettelman, A.,
964 Eaton, B., Boyle, J., Marchand, R. & Ackerman, T.P., 2012. Exposing global cloud bi-
965 ases in the Community Atmosphere Model (CAM) using satellite observations and their
966 corresponding instrument simulators. *Journal of Climate*, 25(15), pp.5190-5207.
- 967 Kay, J. E., Deser, C., Phillips, A., Mai, A., Hannay, C., Strand, G., Arblaster, J.M., Bates,
968 S.C., Danabasoglu, G., Edwards, J. & Holland, M. (2015). The Community Earth Sys-
969 tem Model (CESM) large ensemble project: A community resource for studying climate
970 change in the presence of internal climate variability. *Bulletin of the American Meteorolo-
971 gical Society*, 96(8), 1333-1349.
- 972 Klocke, D., Quaas, J., & Stevens, B. (2013). Assessment of different metrics for physical
973 climate feedbacks. *Climate Dynamics*, 41(5-6), 1173-1185.
- 974 Large, W. G., & Yeager, S. G. (2004). Diurnal to decadal global forcing for ocean and
975 sea-ice models: the data sets and flux climatologies. Boulder: National Center for At-
976 mospheric Research.

- 977 Lawson, R. P., & Gettelman, A. (2014). Impact of Antarctic mixed-phase clouds on cli-
978 mate. *Proceedings of the National Academy of Sciences*, 111(51), 18156-18161.
- 979 Li, J. (2000). Gaussian quadrature and its application to infrared radiation.
980 *Journal of the atmospheric sciences*, 57(5), 753-765. doi: 10.1175/1520-
981 0469(2000)057<0753:GQAIAT>2.0.CO;2
- 982 Massom, R. A., Eicken, H., Hass, C., Jeffries, M. O., Drinkwater, M. R., Sturm, M.,
983 Worby, A.P., Wu, X., Lytle, V.I., Ushio, S. and Morris, K. (2001). Snow on Antarctic
984 sea ice. *Reviews of Geophysics*, 39(3), 413-445.
- 985 Mauritsen, T., Stevens, B., Roeckner, E., Crueger, T., Esch, M., Giorgetta, M., ... & Miko-
986 lajewicz, U. (2012). Tuning the climate of a global model. *Journal of Advances in Mod-
987 eling Earth Systems*, 4(3).
- 988 Meehl, G.A., Covey, C., Taylor, K.E., Delworth, T., Stouffer, R.J., Latif, M., McAvaney, B.
989 and Mitchell, J.F. (2007). The WCRP CMIP3 multimodel dataset: A new era in climate
990 change research. *Bulletin of the American Meteorological Society*, 88(9), pp.1383-1394.
- 991 Mishchenko, M. I. (1994). Asymmetry parameters of the phase function for densely
992 packed scattering grains. *Journal of Quantitative Spectroscopy and Radiative Transfer*,
993 52(1), 95-110.
- 994 Mlawer, E. J., Taubman, S. J., Brown, P. D., Iacono, M. J., & Clough, S. A. (1997). Ra-
995 diative transfer for inhomogeneous atmospheres: RRTM, a validated correlated- k
996 model for the longwave. *Journal of Geophysical Research: Atmospheres*, 102(D14),
997 16663-16682.
- 998 Neftel, A., H. Friedli, E. Moor, H. L   tcher, H. Oeschger, U. Siegenthaler, and B. Stauff-
999 er, 1994, Historical CO2 record from the Siple Station ice core. In Trends: A Com-
1000 pendium of Data on Global Change. Carbon Dioxide Information Analysis Center, Oak
1001 Ridge National Laboratory, U.S. Department of Energy, Oak Ridge, Tenn., U.S.A.
- 1002 NOAA ESRL Global Monitoring Division. 2015, updated annually. Atmospheric Carbon
1003 Dioxide Dry Air Mole Fractions from quasi-continuous measurements at Mauna Loa,
1004 Hawaii. Compiled by K.W. Thoning, D.R. Kitzis, and A. Crotwell. National Oceanic
1005 and Atmospheric Administration (NOAA), Earth System Research Laboratory (ESRL),
1006 Global Monitoring Division (GMD): Boulder, Colorado, USA. Version 2015-12 at
1007 <http://dx.doi.org/10.7289/V54X55RG>.
- 1008 Otto-Bliesner, B. L., Brady, E. C., Fasullo, J., Jahn, A., Landrum, L., Stevenson, S.,
1009 Rosenbloom, N., Mai, A. & Strand, G. (2016). Climate variability and change since 850
1010 CE: An ensemble approach with the community earth system model. *Bulletin of the
1011 American Meteorological Society*, 97(5), 735-754. doi:[http://dx.doi.org/10.1175/BAMS-
1012 D-14-00233.1](http://dx.doi.org/10.1175/BAMS-D-14-00233.1)
- 1013 Park, T. W., Deng, Y., Cai, M., Jeong, J. H., & Zhou, R. (2014). A dissection of the sur-
1014 face temperature biases in the Community Earth System Model. *Climate dynamics*,
1015 43(7-8), 2043-2059.
- 1016 Qu, X., & Hall, A. (2006). Assessing snow albedo feedback in simulated climate change.
1017 *Journal of Climate*, 19(11), 2617-2630.
- 1018 Qu, X., & Hall, A. (2007). What controls the strength of snow-albedo feedback?. *Journal
1019 of Climate*, 20(15), 3971-3981.
- 1020 Qu, X., & Hall, A. (2014). On the persistent spread in snow-albedo feedback. *Climate Dy-
1021 namics*, 42(1-2), 69-81.
- 1022 Sanderson, B. M., Shell, K. M., & Ingram, W. (2010). Climate feedbacks determined us-
1023 ing radiative kernels in a multi-thousand member ensemble of AOGCMs. *Climate Dy-
1024 namics*, 35(7), 1219-1236.
- 1025 Shell, K. M., Kiehl, J. T., & Shields, C. A. (2008). Using the radiative kernel technique
1026 to calculate climate feedbacks in NCAR's Community Atmospheric Model. *Journal of
1027 Climate*, 21(10), 2269-2282.
- 1028 Smith, R., Jones, P., Briegleb, B., Bryan, F., Danabasoglu, G., Dennis, J., Dukowicz, J.,
1029 Eden, C., Fox-Kemper, B., Gent, P. & Hecht, M. (2010). The parallel ocean program
1030 (POP) reference manual ocean component of the community climate system model

- 1031 (CCSM) and community earth system model (CESM). Rep. LAUR-01853, 141.
- 1032 Soden, B. J., Held, I. M., Colman, R., Shell, K. M., Kiehl, J. T., & Shields, C. A. (2008).
- 1033 Quantifying climate feedbacks using radiative kernels. *Journal of Climate*, 21(14), 3504-
- 1034 3520.
- 1035 Stroeve, J., Holland, M. M., Meier, W., Scambos, T., & Serreze, M. (2007). Arctic sea ice
- 1036 decline: Faster than forecast. *Geophysical Research Letters*, 34(9).
- 1037 Taylor, K. E., Stouffer, R. J., & Meehl, G. A. (2012). An overview of CMIP5 and the ex-
- 1038 periment design. *Bulletin of the American Meteorological Society*, 93(4), 485-498.
- 1039 Trenberth, K. E., Fasullo, J. T., & Kiehl, J. (2009). Earth's global energy budget. *Bulletin*
- 1040 *of the American Meteorological Society*, 90(3), 311-323. doi:10.1175/2008bams2634.1
- 1041 Warren, S. G., Rigor, I. G., Untersteiner, N., Radionov, V. F., Bryazgin, N. N., Aleksan-
- 1042 drov, Y. I., & Colony, R. (1999). Snow depth on Arctic sea ice. *Journal of Climate*,
- 1043 12(6), 1814-1829.
- 1044 Warren, S. G., & Brandt, R. E. (2008). Optical constants of ice from the ultraviolet to
- 1045 the microwave: A revised compilation. *Journal of Geophysical Research: Atmospheres*,
- 1046 113(D14).
- 1047 Webster, M. A., Rigor, I. G., Nghiem, S. V., Kurtz, N. T., Farrell, S. L., Perovich, D. K.,
- 1048 & Sturm, M. (2014). Interdecadal changes in snow depth on Arctic sea ice. *Journal of*
- 1049 *Geophysical Research: Oceans*, 119(8), 5395-5406.
- 1050 Wetherald, R. T., & Manabe, S. (1988). Cloud feedback processes in a general circulation
- 1051 model. *Journal of the Atmospheric Sciences*, 45(8), 1397-1416.
- 1052 Winton, M. (2006). Surface albedo feedback estimates for the AR4 climate models. *Jour-*
- 1053 *nal of Climate*, 19(3), 359-365.
- 1054 Zunz, V., Goosse, H., & Massonnet, F. (2013). How does internal variability influence
- 1055 the ability of CMIP5 models to reproduce the recent trend in Southern Ocean sea ice
- 1056 extent? *The Cryosphere*, 7(2), 451-468.

Table 1. RRTMG_LW Bands and Surface Emissivity values

RRTMG_LW		Emissivity		
Band	Limits (cm ⁻¹)	Snow	Ocean	Desert
1	10-350	0.9936	0.8488	0.9116
2	350-500	0.9883	0.8845	0.8866
3	500-630	0.9799	0.8874	0.9055
4	630-700	0.9717	0.899	0.9591
5	700-820	0.9643	0.9189	0.9605
6	820-980	0.982	0.9531	0.9376
7	980-1080	0.9862	0.9502	0.8783
8	1080-1180	0.9909	0.9447	0.9181
9	1180-1390	0.9812	0.9400	0.9780
10	1390-1480	0.9776	0.9362	0.9741
11	1480-1800	0.9771	0.9359	0.9705
12	1800-2080	0.9717	0.9374	0.9676
13	2080-2250	0.965	0.9349	0.9648
14	2250-2380	0.9636	0.9336	0.9648
15	2380-2600	0.9583	0.9316	0.9636
16	2600-3250	0.9391	0.9251	0.9613
Planck-averaged broadband		0.982	0.901	0.922
CESM1 broadband		0.970	1.000	0.960

Table 2. Sea-ice emissivity globally-averaged feedbacks [$\text{W}/\text{m}^2/\text{K}$]. See text for further details.

$\Delta\bar{T}_S$	Sky	Case	Kernel	
			Static	Time-dependent/Dynamic
Global Mean	Clear	HISTCO2	$3.27 \times 10^{-2} \pm 1.49 \times 10^0$	$3.05 \times 10^{-2} \pm 2.29 \times 10^{-3}$
		2 $\times\text{CO}_2$, RCP 8.5 2065	$1.75 \times 10^{-2} \pm 1.28 \times 10^{-3}$	$1.55 \times 10^{-2} \pm 3.46 \times 10^{-4}$
		RCP 2.6 2100	$1.71 \times 10^{-2} \pm 1.31 \times 10^{-3}$	$1.52 \times 10^{-2} \pm 3.50 \times 10^{-4}$
		RCP 8.5 2100	$1.67 \times 10^{-2} \pm 7.54 \times 10^{-4}$	$1.43 \times 10^{-2} \pm 1.95 \times 10^{-4}$
	All	HISTCO2	$1.50 \times 10^{-2} \pm 1.16 \times 10^0$	$8.15 \times 10^{-3} \pm 1.63 \times 10^{-3}$
		2 $\times\text{CO}_2$, RCP 8.5 2065	$9.53 \times 10^{-3} \pm 1.28 \times 10^{-3}$	$5.44 \times 10^{-3} \pm 2.56 \times 10^{-4}$
		RCP 2.6 2100	$9.22 \times 10^{-3} \pm 1.32 \times 10^{-3}$	$5.38 \times 10^{-3} \pm 2.53 \times 10^{-4}$
		RCP 8.5 2100	$9.46 \times 10^{-3} \pm 7.70 \times 10^{-4}$	$4.79 \times 10^{-3} \pm 1.95 \times 10^{-4}$
Zonal Mean	Clear	HISTCO2	$8.49 \times 10^{-3} \pm 2.05 \times 10^{-3}$	$8.06 \times 10^{-3} \pm 1.92 \times 10^{-3}$
		2 $\times\text{CO}_2$, RCP 8.5 2065	$9.19 \times 10^{-3} \pm 3.47 \times 10^{-4}$	$8.19 \times 10^{-3} \pm 2.38 \times 10^{-4}$
		RCP 2.6 2100	$9.03 \times 10^{-3} \pm 3.28 \times 10^{-4}$	$8.11 \times 10^{-3} \pm 2.32 \times 10^{-4}$
		RCP 8.5 2100	$9.26 \times 10^{-3} \pm 2.40 \times 10^{-4}$	$8.05 \times 10^{-3} \pm 1.47 \times 10^{-4}$
	All	HISTCO2	$3.71 \times 10^{-3} \pm 2.01 \times 10^{-1}$	$2.32 \times 10^{-3} \pm 2.01 \times 10^{-1}$
		2 $\times\text{CO}_2$, RCP 8.5 2065	$4.55 \times 10^{-3} \pm 3.77 \times 10^{-4}$	$2.77 \times 10^{-3} \pm 2.39 \times 10^{-4}$
		RCP 2.6 2100	$4.44 \times 10^{-3} \pm 6.99 \times 10^{-4}$	$2.75 \times 10^{-3} \pm 3.92 \times 10^{-4}$
		RCP 8.5 2100	$4.82 \times 10^{-3} \pm 2.74 \times 10^{-4}$	$2.62 \times 10^{-3} \pm 1.52 \times 10^{-4}$

1059 **Figure 1.** Focusing on Arctic ocean latitudes, a) comparison of 1979-2005 Arctic surface temperatures
1060 monthly and spatially-averaged over 69°-90° North for CESM- $\epsilon(\nu)$ (red), the mean of 10 fully-forced CESM-
1061 LME models (green), and ERA-Interim skin temperature reanalysis (blue), b) the residuals with respect to
1062 ERA-Interim skin temperature for CESM - $\epsilon(\nu)$ radiative surface temperature (red) and CESM-LME (green),
1063 c) December-January-February residuals for the same period and region where error bars show the deviations
1064 over the months, and d) are the June-July-August residuals for the same period and region.

1065 **Figure 2.** North Pole projection difference maps of Arctic radiative surface temperatures in the period
1066 1979-2005 over 60°-90° northern latitudes. Skin temperature reanalysis data is from ERA-Interim (*Dee*
1067 *et al* [2011]), CESM-LME is the 10 ensemble mean of historical 20th century fully-forced model from the
1068 CESM Last Millenium Ensemble (*Otto-Bliesner et al.* [2016]), and CESM- $\epsilon(\nu)$ is this work's model, for the
1069 HISTCO2 case. December-January-February (DJF) mean surface temperature differences are plotted between
1070 a) CESM- $\epsilon(\nu)$ and ERA-Interim, b) CESM-LME and ERA-Interim and c) CESM- $\epsilon(\nu)$ -CESM-LME. d), e)
1071 and f) show the same for months June-July-August (JJA). Crosses indicate statistically significant grid points
1072 to $p < 0.05$ of the Welch's t-test.

1073 **Figure 3.** For the RCP 8.5 case, end of century 10-year averaged clear-sky ϵ kernel maps for four seasons:
1074 a) December-January-February, b) March-April-May, c) June-July-August, and d) September-October-
1075 November.

1076 **Figure 4.** Same description as Figure 3, except for all-sky.

1077 **Figure 5.** Emissivity difference in RRTMG_LW band 6 between 10-year average in RCP8.5 end of century
1078 and a 10-year average of 1850CNTL, for four seasons: a) December-January-February, b) March-April-May,
1079 c) June-July-August, and d) September-October-November. Red regions denote increased emissivity and in
1080 blue areas, the emissivity has reduced.

1081 **Figure 6.** Globally- and temporally-averaged spectral kernel amplitudes by RRTMG_LW band, for the last
1082 10 years end-of-century RCP 8.5 case for a) clear- and b) all-sky. c) The globally- and temporally-averaged
1083 spectral emissivity change of the last 10-years of RCP 8.5 and 10 years of 1850CNTL.

1084 **Figure 7.** Temporal evolution of emissivity kernels and climatological emissivity change. a) Solid lines
 1085 show globally-averaged broadband clear-sky ϵ kernel strength in units of $\text{W/m}^2/\epsilon$. Dotted lines are polyno-
 1086 mial fits to the clear-sky kernels. Dashed lines are ratios of all-sky to clear-sky globally-averaged broadband
 1087 ϵ kernel amplitudes and is unitless. b) Globally-averaged broadband emissivity change with respect to the
 1088 1850CNTL case.

1089 **Figure 8.** Broadband kernel reduction for forced CO_2 atmosphere cases, with respect to the 1850CNTL
 1090 case. a) and b) are clear-sky kernel reductions area-averaged in northern and southern high latitudes, respec-
 1091 tively. c) and d) show the all-sky cases area-averaged in northern and southern high latitudes, respectively.

1092 **Figure 9.** Total precipitable water and total cloud fraction for forced CO_2 atmosphere cases. a) and b)
 1093 Area-averaged in northern and southern high latitude total precipitable water, respectively. c) and d) show
 1094 area-averaged total cloud fraction in northern and southern high latitudes, respectively.

1095 **Figure 10.** Spectral ϵ kernels for RCP8.5 scenario in high northern latitudes a) clear and b) all-sky, and in
 1096 high southern latitudes d) clear- and e) all-sky, on a monthly basis. The color scheme for RRTMG_LW bands
 1097 is [red, green, blue, yellow] for bands=[1,2,3,4] and repeated 3 more times up to band 16.

1098 **Figure 11.** Average spectral climatological surface ϵ change on a monthly basis between 2090-2100 in
 1099 RCP8.5 scenario and 10 years of 1850CNTL for a) high northern latitudes and b) high southern latitudes. Av-
 1100 erage seasonal month-to-month surface ϵ change in years 2090-2100 of RCP8.5 scenario for c) high northern
 1101 latitudes and d) high southern latitudes. See Eqns. 5 and 6 for $\Delta\epsilon_i$ and $\delta\epsilon_i$ definitions.

1102 **Figure 12.** Zonally-averaged emissivity feedback of cryosphere for each of the four CO_2 forced cases, rela-
 1103 tive to 1850CNTL. Kernels from 1850CNTL atmosphere were used in this case, with clear-sky on the left and
 1104 all-sky on the right plot. Normalization by global mean $\Delta\bar{T}_S$, for conventional prescription of feedback. The
 1105 HISTCO2 feedback is large due to smaller global mean $\Delta\bar{T}_S$.

1106 **Figure 13.** Sea-ice emissivity feedbacks calculated using different reference periods and kernel types (static
1107 or time-dependent/dynamic). a) Comparison of 2 different reference periods, each using their respective static
1108 kernel. b) For the same reference period, comparison of feedback using static kernel vs. dynamic kernel. c)
1109 Comparison of 2 different reference periods, each using their respective dynamic kernels. d) Comparison of 2
1110 different reference periods, each using their respective dynamic kernels, but feedback is normalized by zonal
1111 mean temperature. Marker colors indicate the model case, as described in other figures in this manuscript.
1112 Marker fill styles indicate: left fill-clear sky Northern Hemisphere (NH), right fill-all sky NH, bottom fill-
1113 clear sky southern hemisphere (SH), top fill-all sky SH, full fill-clear sky global, no fill-all sky global. The
1114 line of agreement is the black dashed line, and the blue line is a linear regression.

1115 **Figure 14.** Climatological surface ϵ feedback, calculated with time-dependent kernels of outgoing long-
1116 wave radiation sensitivity to surface emissivity and zonally-averaged surface temperature change, relative to
1117 10-year averages in 1850CNTL. Error bar lengths indicate uncertainties propagated from standard deviations
1118 in kernel, surface emissivity, and surface temperature values.

1119 **Figure 15.** RRTMG_LW band 6 seasonal emissivity radiative response factors for high sea-ice domi-
1120 nant latitudes. a) northern and d) southern high latitude monthly emissivity kernels for the last 10 years of
1121 each case, the last year noted in the figure legend. b) northern and e) southern high latitude month-to-month
1122 emissivity change ($\delta\epsilon_{i=6}$, Eqn. 6). c) northern and f) southern high latitude emissivity radiative response.
1123 Errorbars are calculated from the 10-year variability. Kernel and radiative response plots use solid lines for
1124 clear-sky, and dashed lines for all-sky.

1125
1126
1127

Figure 16. Zonally- and time-averaged seasonal emissivity radiative response for each case, using a) clear-sky kernels, and b) all-sky kernels. The time-average is over 10-year periods ending in the year denoted in the figure legend for each case.

Figure 1.

Author Manuscript

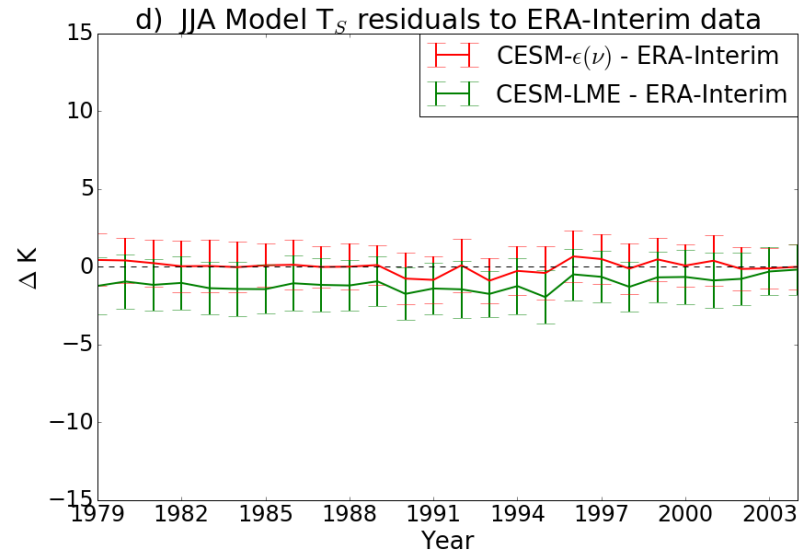
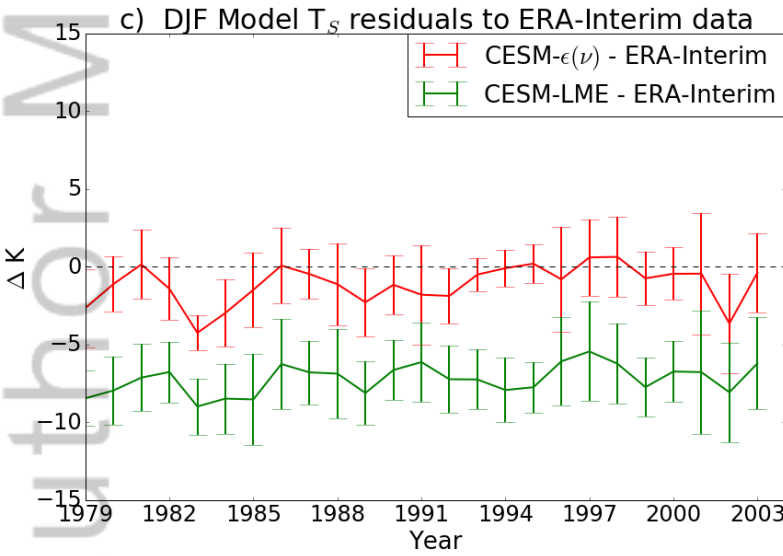
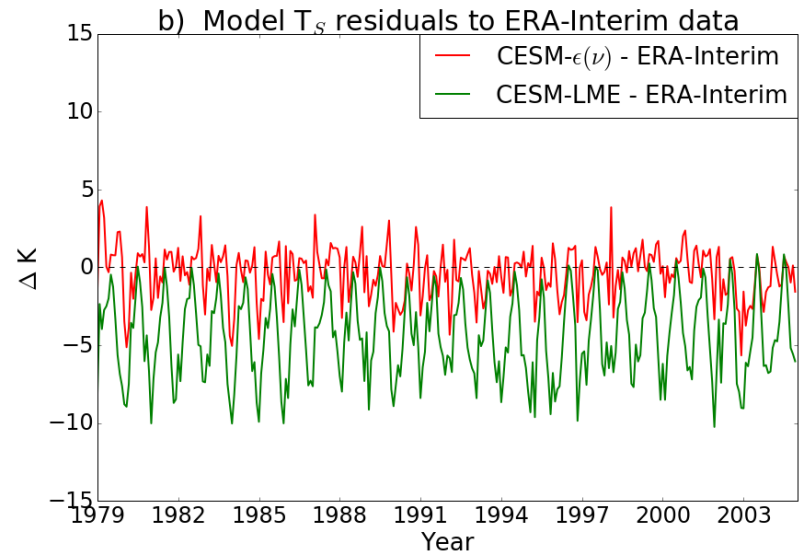
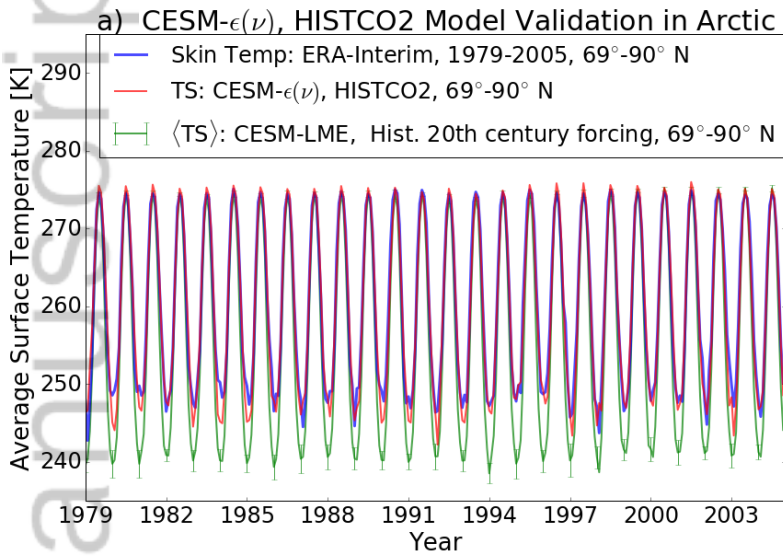


Figure 2.

Author Manuscript

Arctic $\Delta\langle T_S \rangle$ over 1979-2005

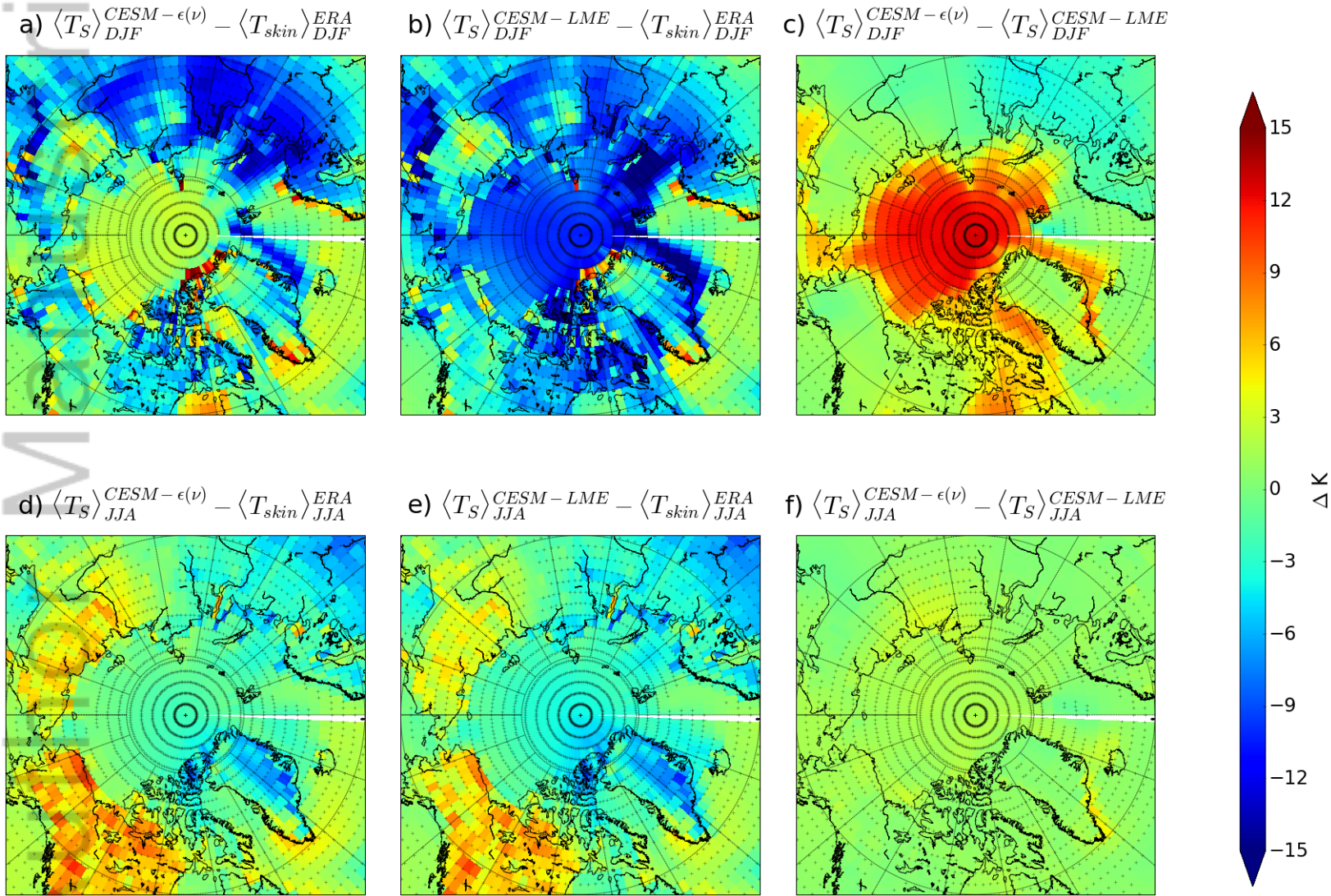


Figure 3.

Author Manuscript

Clear-sky Broadband ϵ Kernel RCP 8.5, 2090-2100

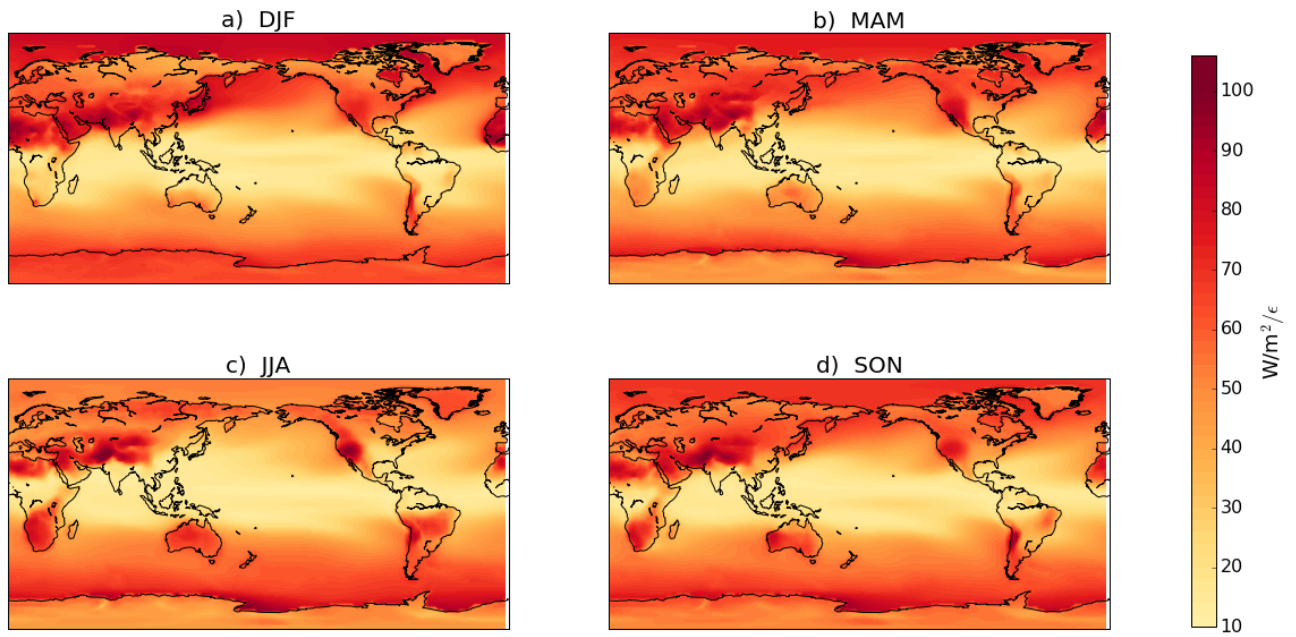


Figure 4.

Author Manuscript

All-sky Broadband ϵ Kernel RCP 8.5, 2090-2100

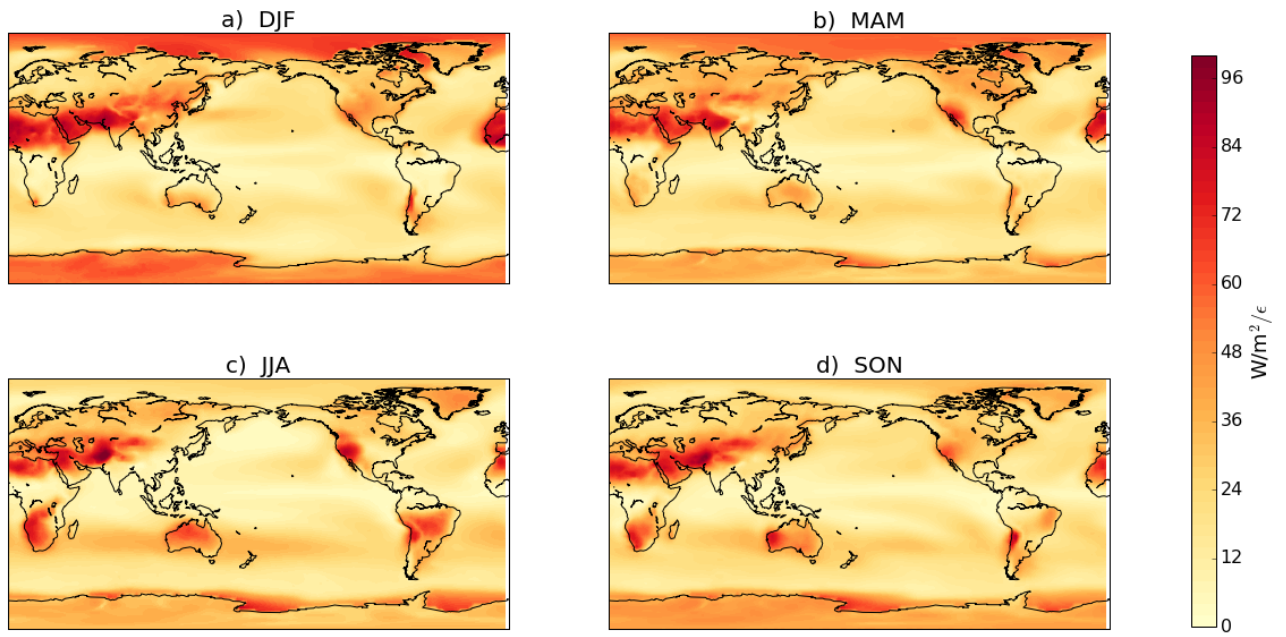


Figure 5.

Author Manuscript

$\Delta\epsilon_{i=6}$ RCP8.5 2090-2100

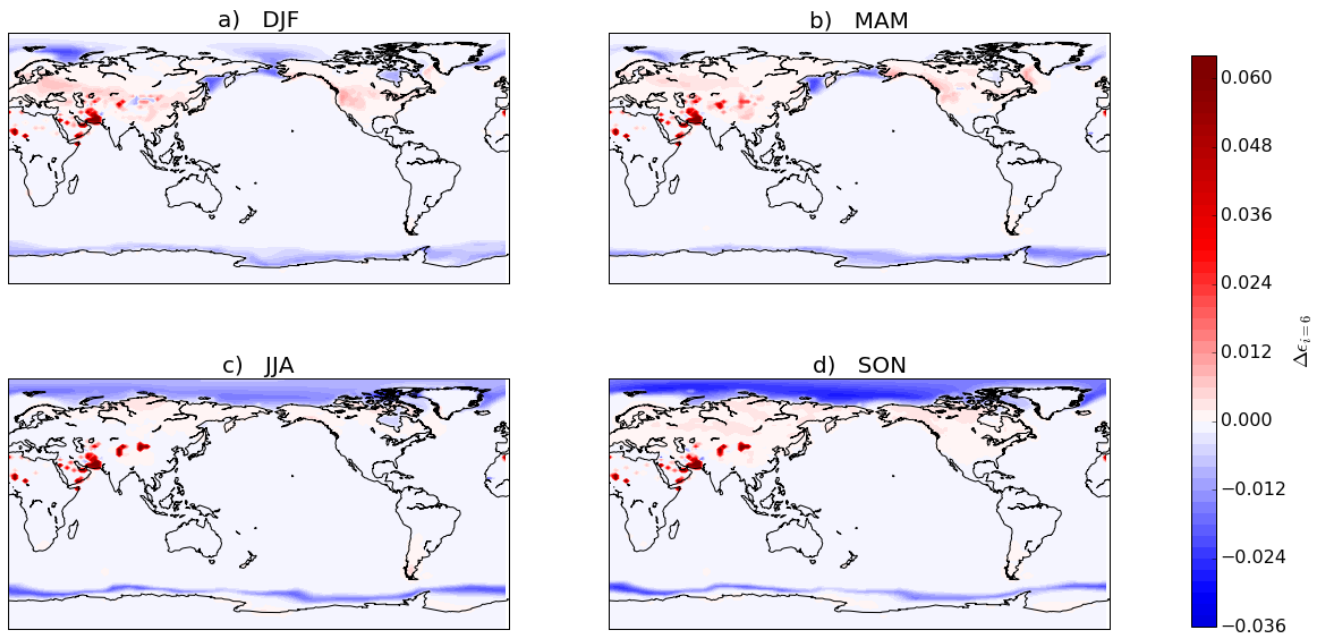


Figure 6.

Author Manuscript

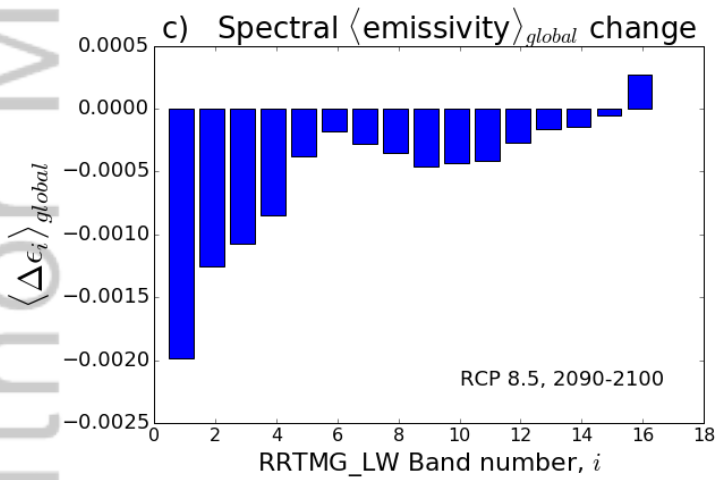
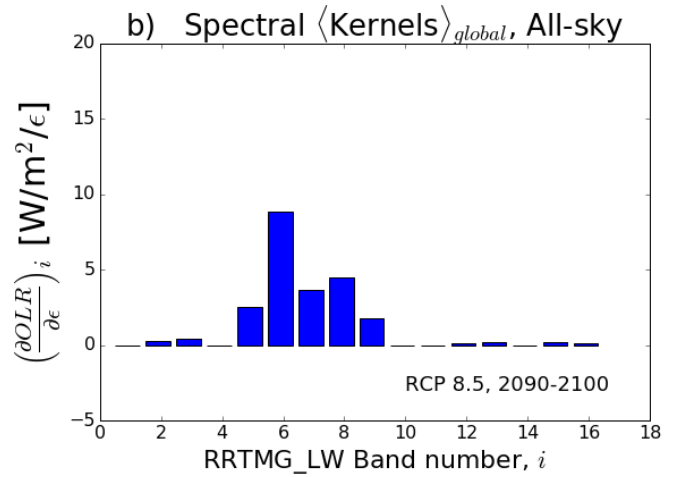
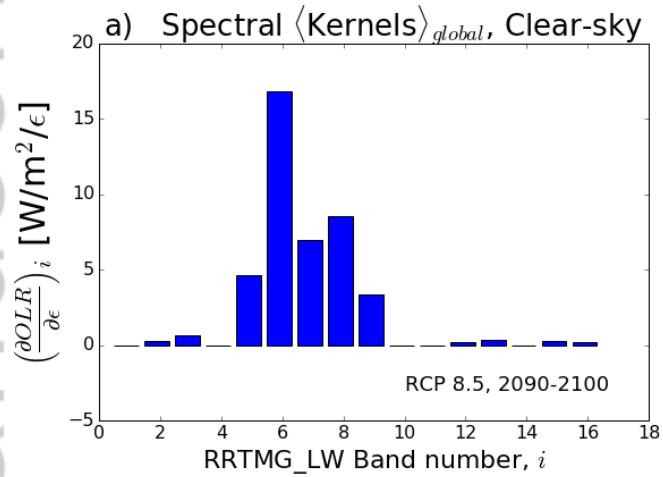
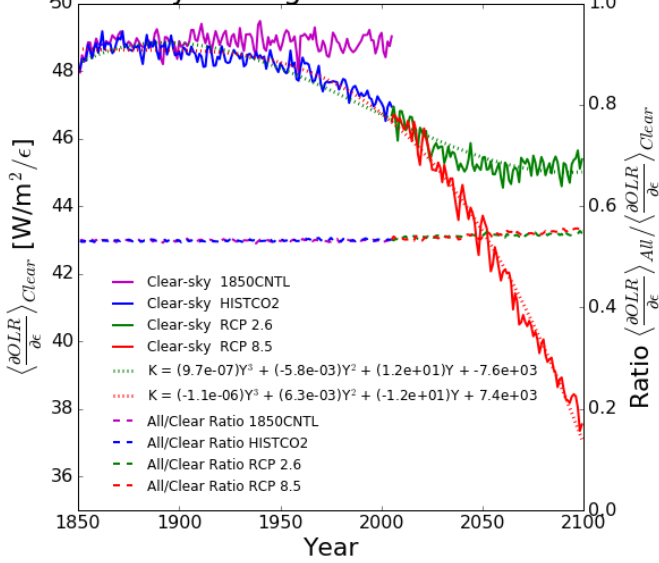


Figure 7.

Author Manuscript

a) Globally-averaged Broadband ϵ Kernel



b) Globally-averaged Broadband $\Delta\epsilon$

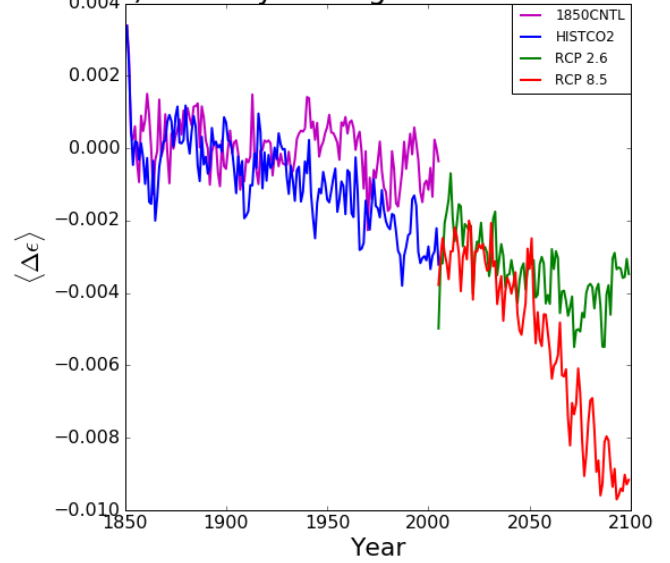


Figure 8.

Author Manuscript

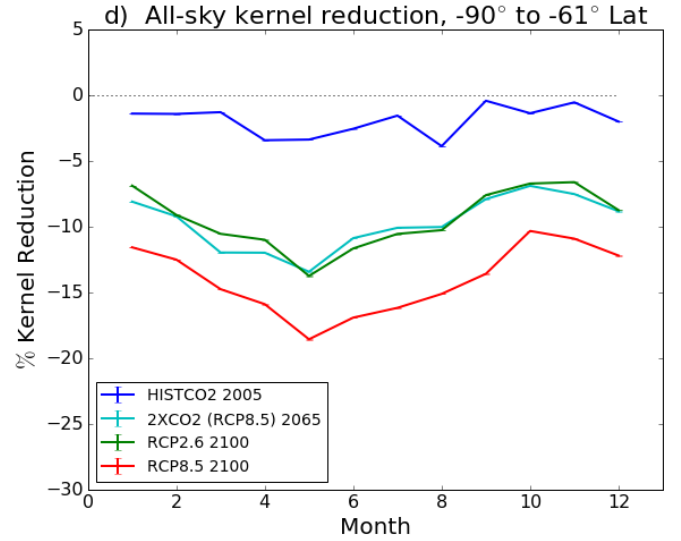
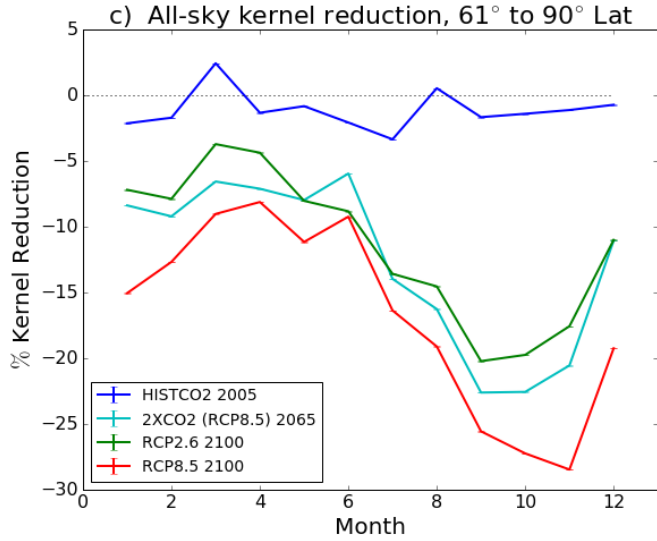
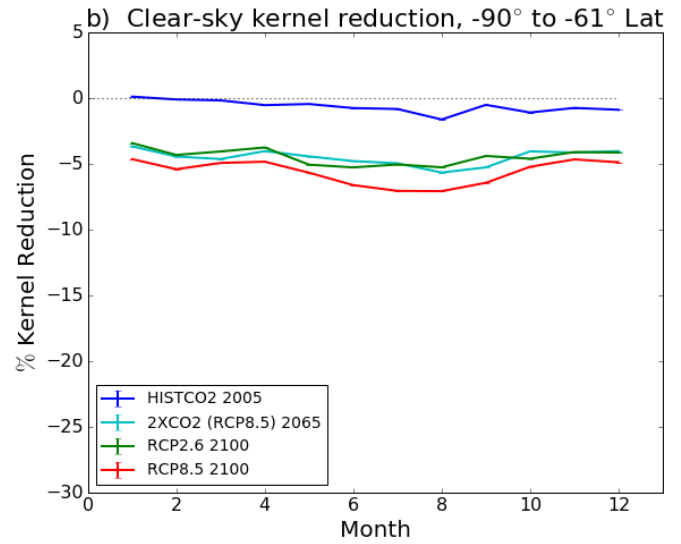
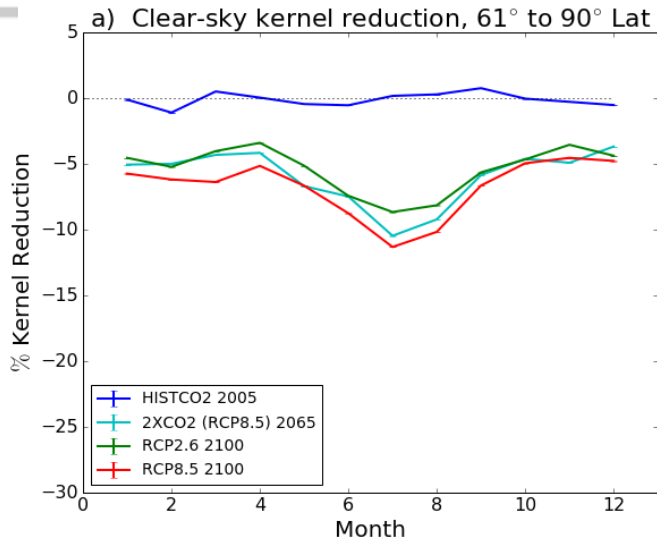


Figure 9.

Author Manuscript

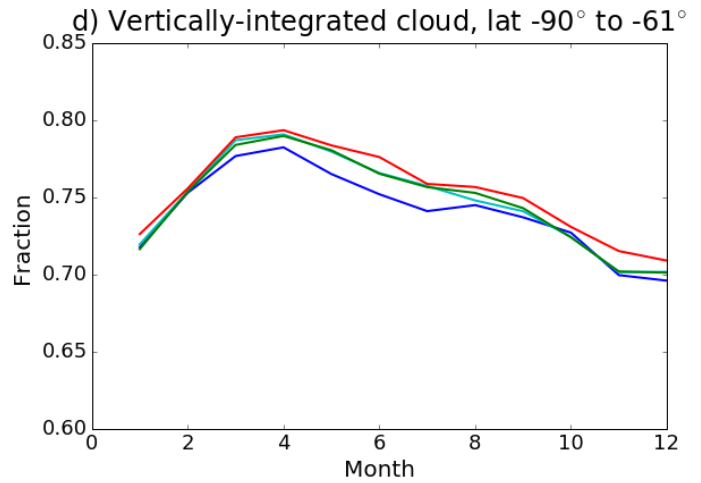
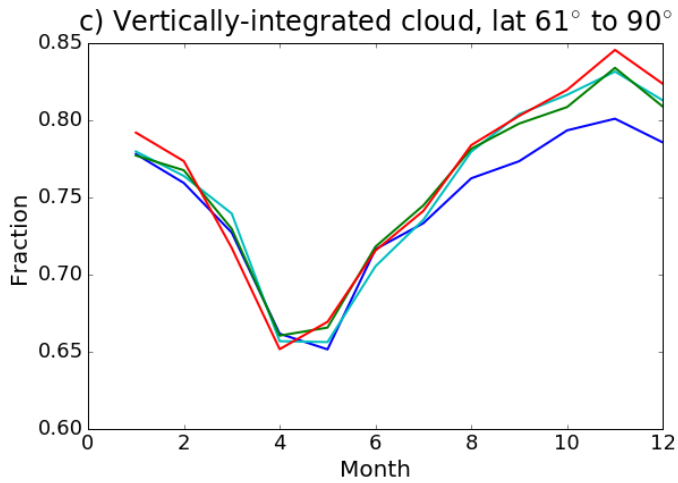
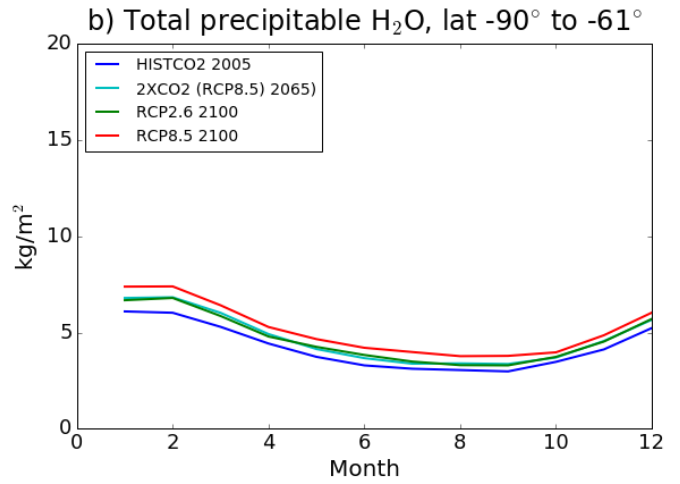
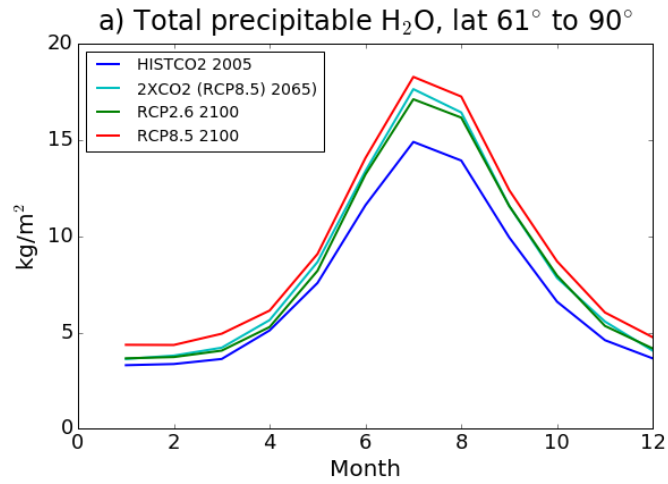
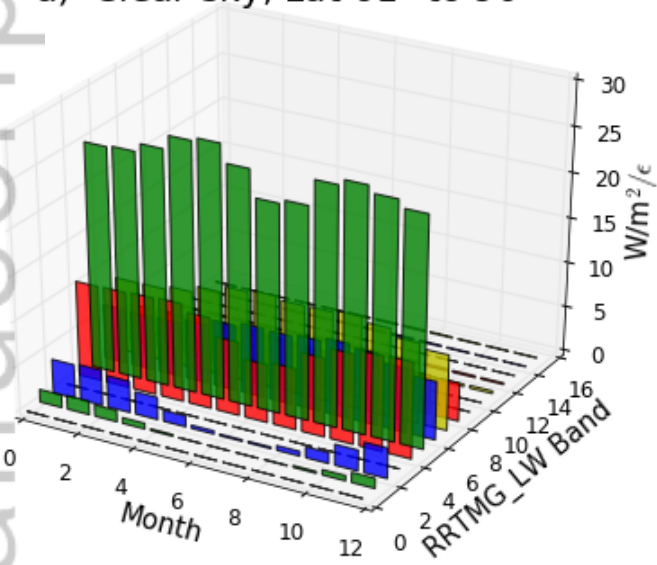


Figure 10.

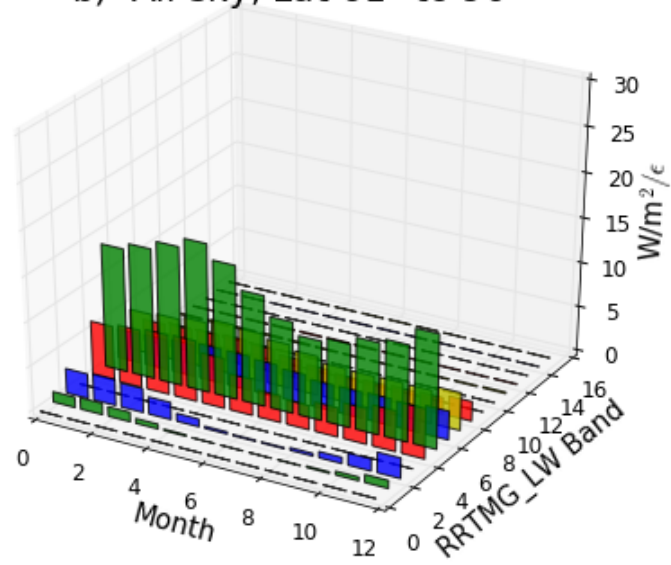
Author Manuscript

RCP 8.5 2090-2100 Kernels

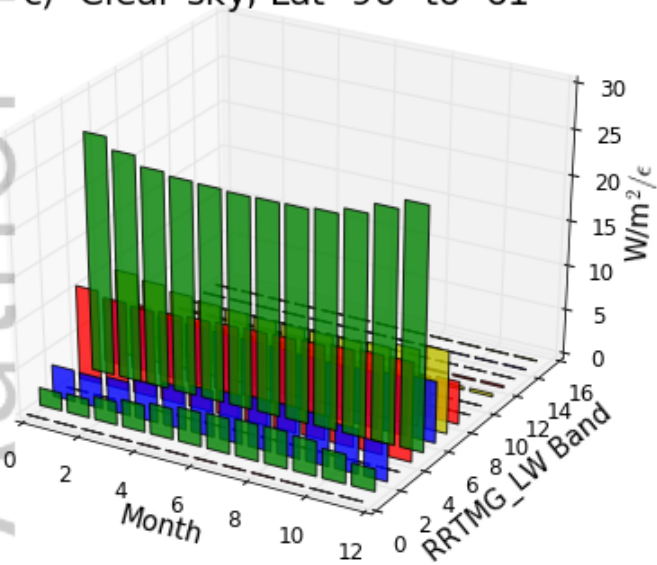
a) Clear-sky, Lat 61° to 90°



b) All-sky, Lat 61° to 90°



c) Clear-sky, Lat -90° to -61°



d) All-sky, Lat -90° to -61°

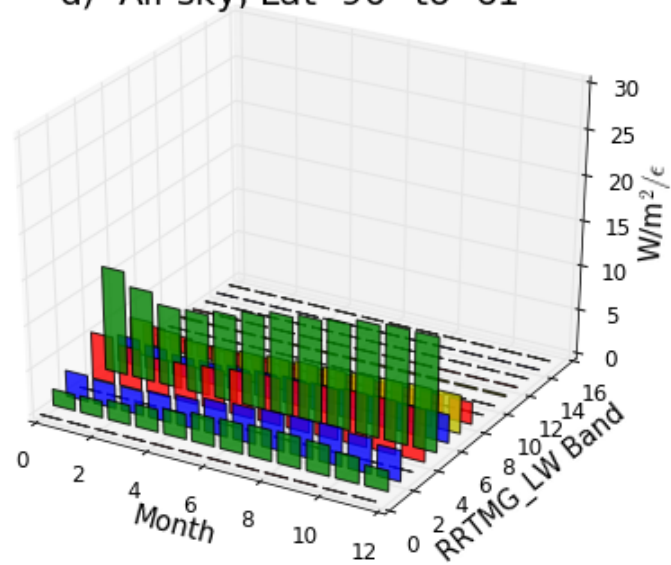


Figure 11.

Author Manuscript

$\epsilon_i(t)$ Change, RCP 8.5 2090-2100

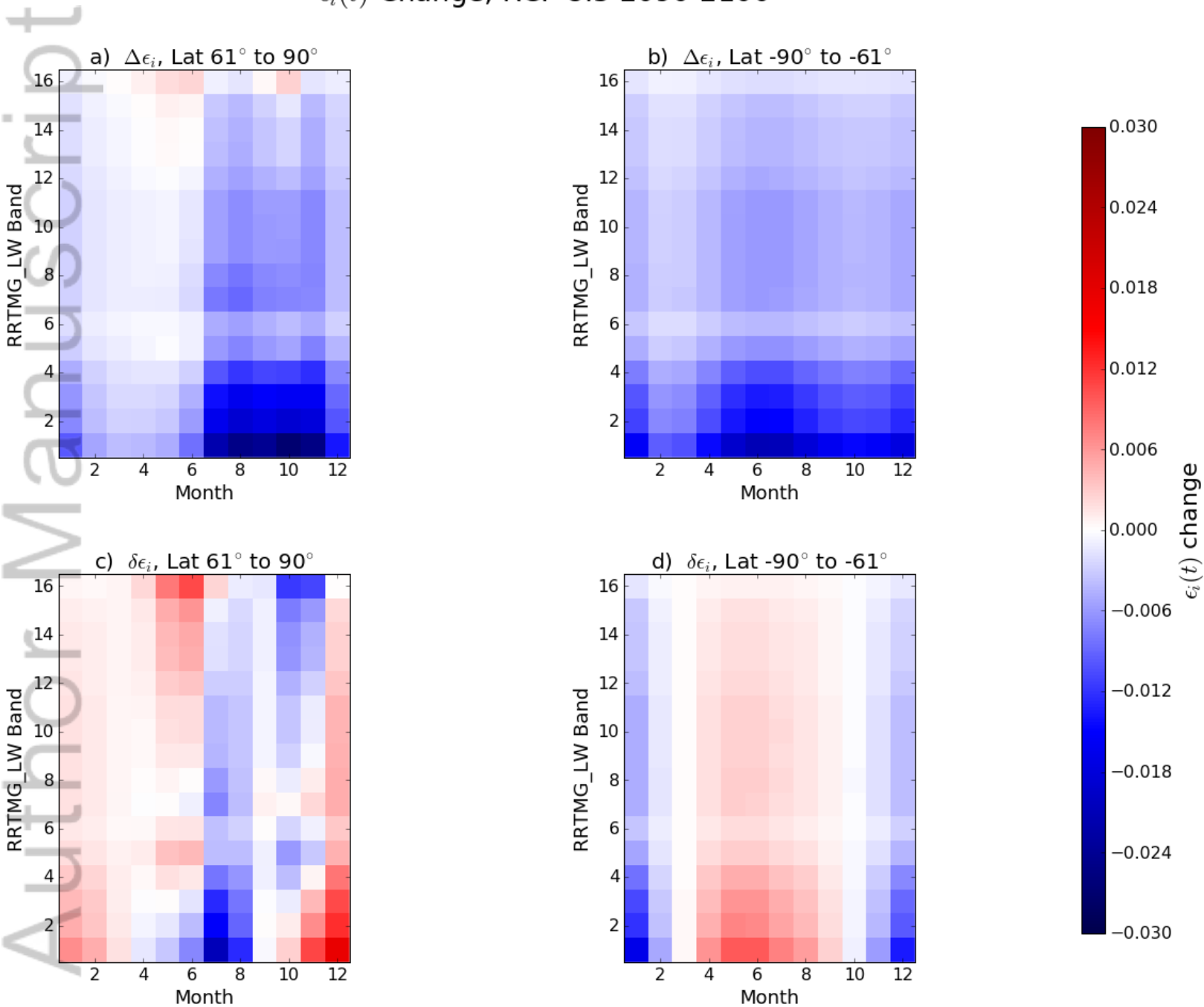


Figure 12.

Author Manuscript

Cryosphere Zonal Emissivity Feedback

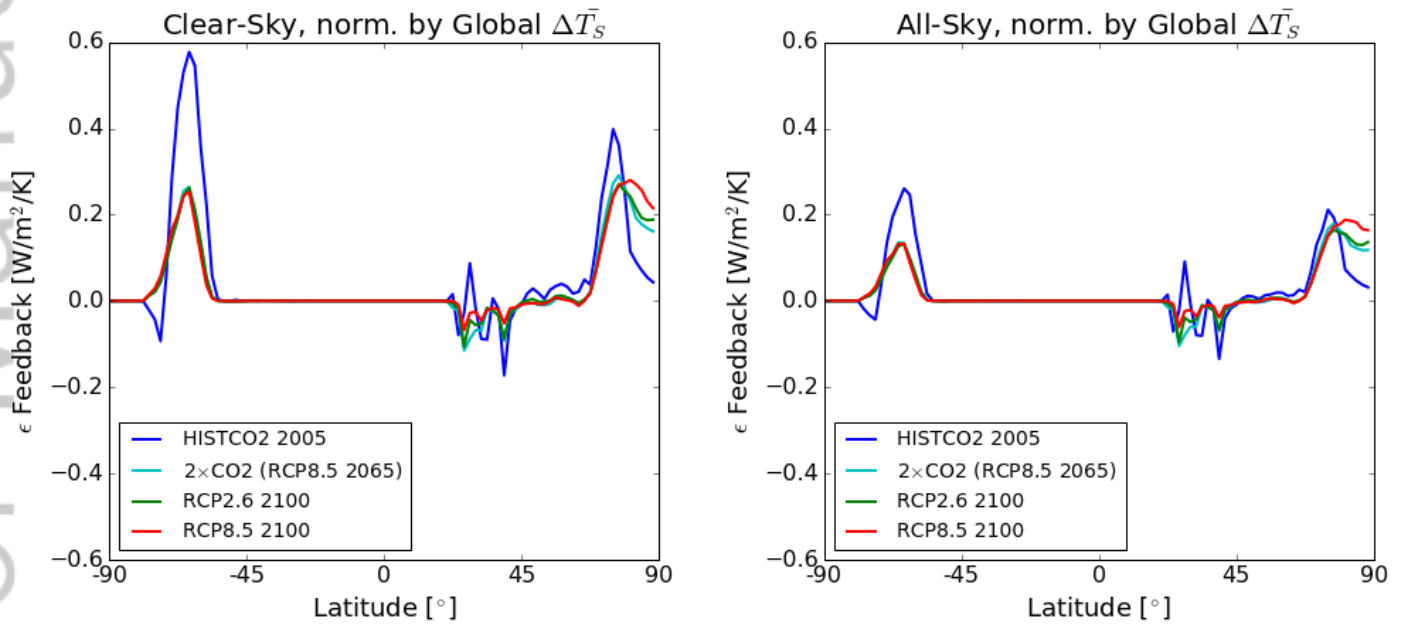
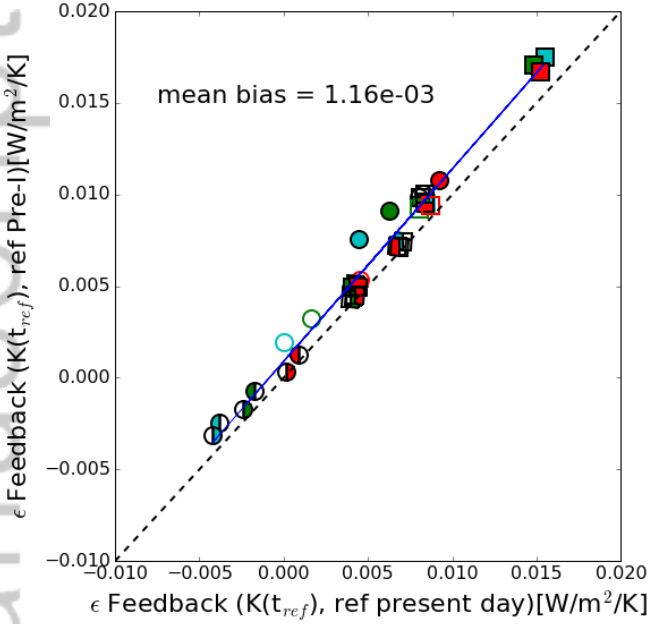


Figure 13.

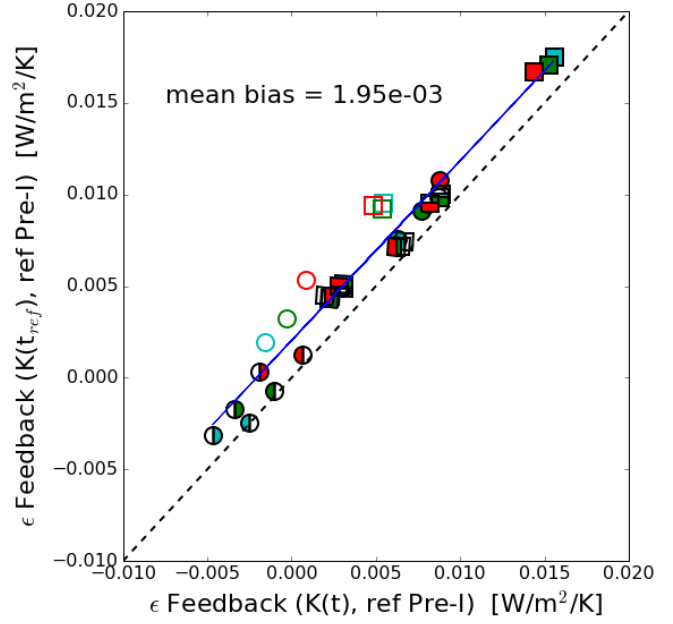
Author Manuscript

ϵ Feedback Calculations: Static vs. Dynamic Kernels

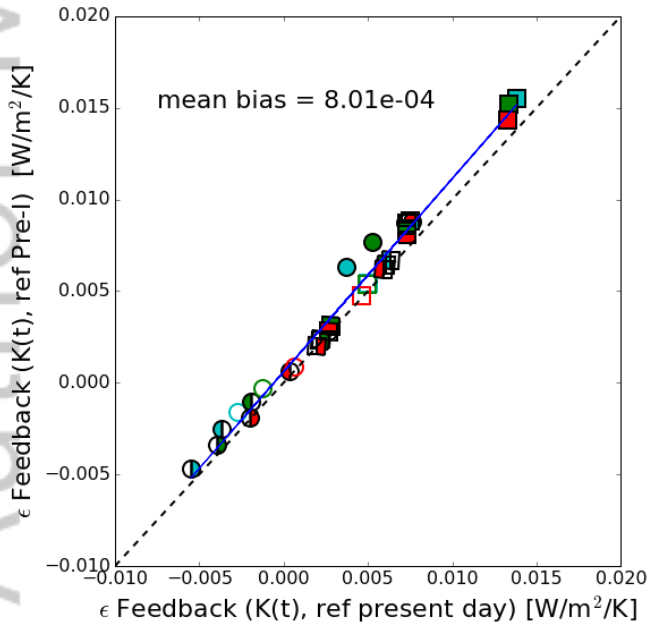
a) Static Kernel, Diff Ref Periods, Global ΔT_S



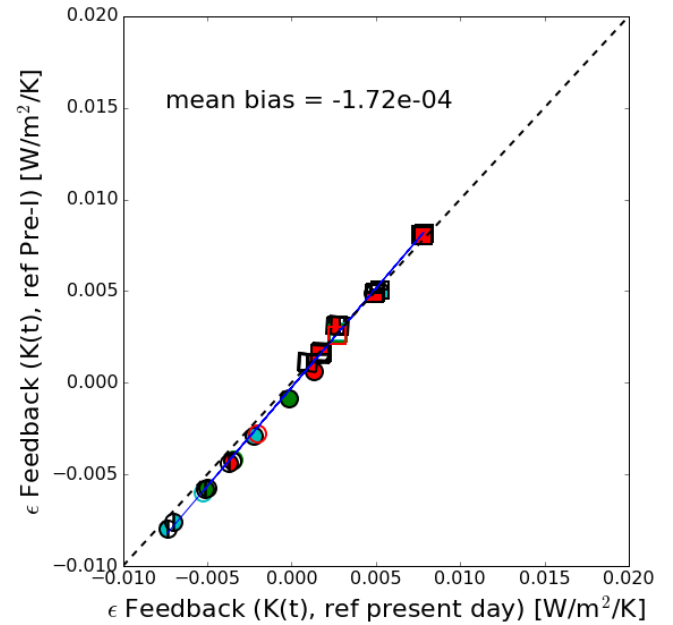
b) Static vs. Dynamic Kernel, Same Ref Period, Global ΔT_S



c) Dynamic Kernel, Diff Ref Periods, Global ΔT_S

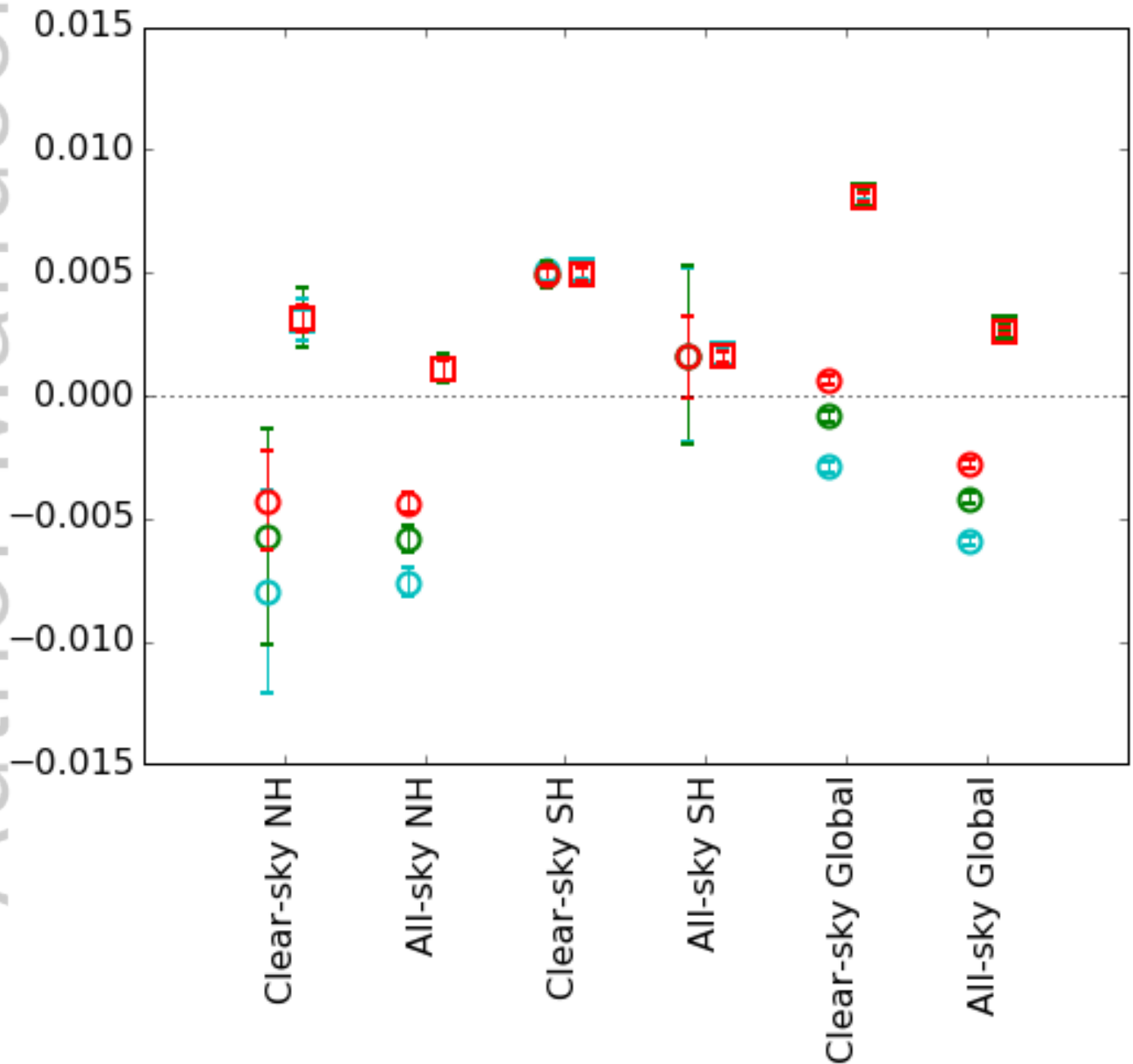


d) Dynamic Kernel, Diff Ref Periods, Zonal ΔT_S





Climatological surface ϵ Feedback



Seasonal Sea-ice ϵ Radiative Response Contributions, Band 6

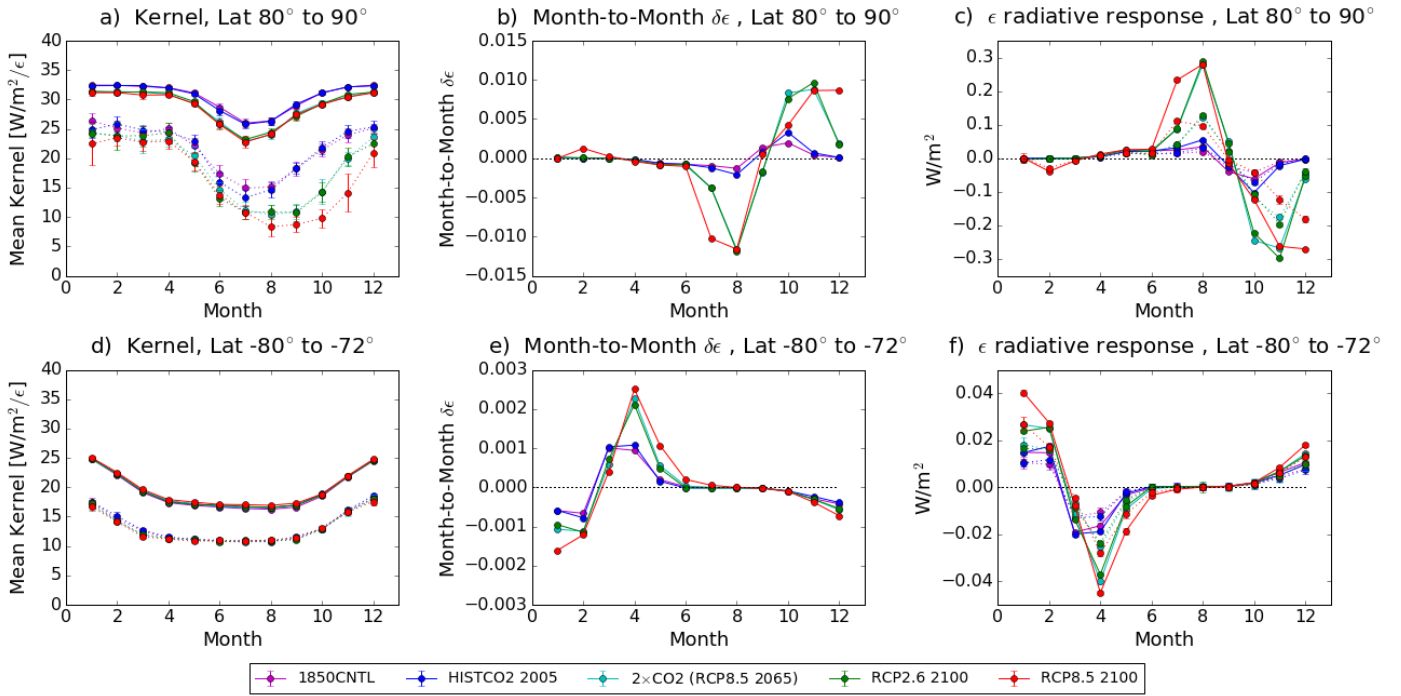


Figure 16.

Author Manuscript

Annually-averaged Seasonal Emissivity Radiative Response

